Design of a 6-DoF vibration isolated frame with active piezoelectric damping

Author
T.F. Haan

Graduation Committee
Dr.Ir. W.B.J. Hakvoort
Ir. B. Seinhorst
Ir. R. Buitenhuis
Dr. Di Maio

Master Thesis
Faculty of Engineering Technology
Master Programme of Mechanical Engineering
Department of Precision Engineering

October, 2024

University of Twente

Abstract

Performance of precision mechanisms in the high-tech industry is limited by disturbing vibrations. Over the last years, developments have been made in the use of piezoelectric patches, integrated with flexures, in order to actively suppress vibrations in various structures. By interconnecting the patches with a positive position feedback (PPF) controller, Seinhorst et al. showed the potential of suppressing parasitic eigenfrequencies. This work aims to extend this technique to a 6 degrees of freedom problem, where the goal is to suppress the nominal eigenfrequencies of a flexure-based vibration isolation system. The active approach does not suffer from the trade-off inherent to passive damping; where vibrations at eigenfrequency are suppressed at the cost of deteriorating performance at higher frequencies. In this work a flexure based isolation system is designed with 6 integrated piezoelectric sensors and actuators in the form of a bimorph flexure, with the nominal suspending frequencies between 10-22 Hz. Using system identification in the frequency domain and structured parameter estimation, the mode shapes and state-space matrices are derived. Using modal decoupling the 6 DoF MIMO control problem is transformed to 6 SISO problems. For each nominal mode, a PPF controller is tuned. The active vibration suppression scheme was implemented successfully, increasing modal damping from 1% to 13%. The results support and highlight the potential of implementing piezoelectric damping in many other industrial cases.

Acknowledgements

I would like to express my heartfelt gratitude to those who have supported me throughout this project.

First and foremost, I extend my sincere thanks to Tim for his invaluable assistance with the mechanical design. Without his expertise, I would not have been able to build a successful setup.

I am also grateful to Ywan for his guidance during the assembly phase. His problem-solving skills and practical tips were instrumental in overcoming assembly challenges.

A special thanks to Ruben for his guidance throughout the entire process. Not only on the contents side was your advise and feedback appreciated, but also on the mental side and finding the right work-life balance.

Finally, I would like to thank to Bram and Wouter. Bram, I appreciated the quick responses to any questions, and the time you would take to help me understand not only your work, but also the problems I needed to solve. Wouter, thanks for your guidance and feedback. You were able to pin-point the most important aspects and problems needing solving, and reduced my worries about the smaller problems along the way.

Thank you all for your contributions and encouragement!

Contents

1 Introduction

In precision mechanisms, undesired vibrations are a key performance limiting factor. As a consequence, a substantial amount of research has been performed with the aim of developing techniques and solutions to limit the influence of disturbing vibrations. Active vibration suppression, where sensors and actuators are used along with control theory to add vibration attenuation to the structure, is one such area that continues to be studied extensively. In 2022, Seinhorst et al. proposed a design method for using piezoelectric patches integrated in flexures for the suppression of parasitic resonances using positive position feedback (PPF) [16]. The technique proved effective for the case of parasitic resonances in a large range of motion flexure mechanism. The work in this thesis is an extension of the technique, by implementing it in a multi-degree-of-freedom setting. In a cooperation between 'DEMCON high-tech systems Delft B.V.' and the University of Twente, we research how this technique can be adapted and applied in an industrially relevant setting.

DEMCON high-tech systems Delft B.V. is a company that develops solutions for various clients in the high-tech industry. In the case considered, performance of the system is limited by vibrations of the metrology frame. The system is illustrated in Figure 1.1. The system has to precisely position the short stroke stage with respect to the optics frame, in order for the machine to be able to perform its function. Hence, the key performance target is to minimise the positioning error. The metrology frame consists of sensors that measure the position of the short stroke stage with respect to the optics frame. The metrology frame is rigidly attached to the optics frame. In order to minimise the impact of vibrations caused by the actuation of the short stroke stage, the optics frame and metrology frame are decoupled from the force frame by a six degree of freedom compliant mechanism with an eigenfrequency between 10-20 Hz. The influence of floor vibrations is suppressed by isolator legs with an eigenfrequency of 1Hz. In evaluation of the system performance, the largest error source is found to be due to actuator to sensor vibrations that excite the metrology frame at the eigenfrequency between 10-20 Hz. The aim of this work is to demonstrate that the use of piezoelectric patches along with active vibration suppression is a suitable method for damping these vibrations, thus improving the performance of the system. The potential performance of this method will be evaluated on a demonstrator setup, which consists of the short stroke mechanism placed on an optical table. The design, assembly, control and validation of the metrology frame and suspension mechanism are part of this thesis.

Piezoelectric patches are used as actuators and sensors for the active vibration suppression of the metrology frame. Through the piezoelectric effect, mechanical stresses generate an electrical charge on the patch [9]. The straining of the patch causes the positive and negative charge centers of unit cells of the material to move, the material has become polarized. As a consequence, surface charge is accumulated on opposing sides of the material, which leads to a measurable voltage difference across the piezoelectric material. The inverse piezoelectric effect is the reverse of this process, a voltage difference applied over the material leads to a mechanical strain of the piezoelectric. As such, a piezoelectric patch can function as both a sensor to detect strain, and as an actuator. A piezoelectric bimorph is created by sandwiching a leaf flexure in between two piezoelectric patches, depicted schematically in Figure 1.2. Contraction of the piezoelectric patch on one side will cause the leaf flexure to bend. The second piezoelectric patch can be used to sense the bending of the flexure. Thus, a piezoelectric bimorph functions as a collocated actuator-sensor pair. The low build volume and ease of integration make them naturally attractive to use as actuators and sensors for flexure-based mechanisms.

The block diagram, in Figure 1.3, highlights the control problem in which the bimorphs

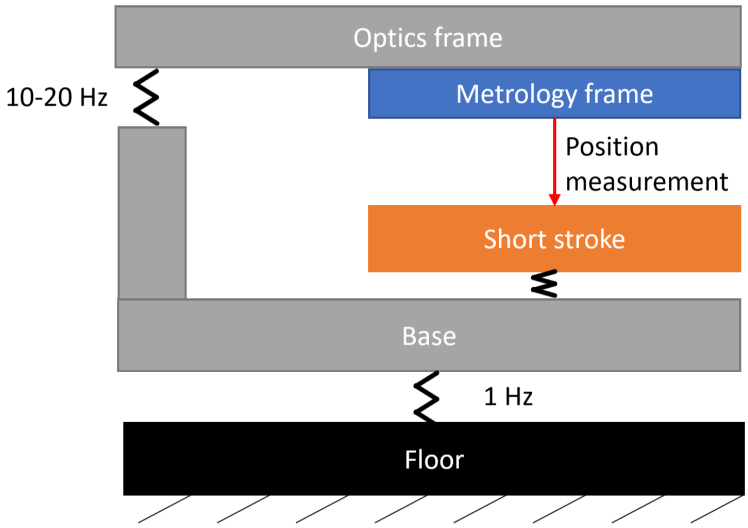

Figure 1.1: Overview of the system for which the active vibration control solution is investigated. The vibrations at the eigenfrequency of the suspension between the base and the optics frame need to be suppressed.

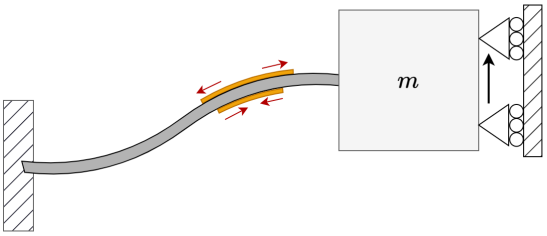

Figure 1.2: Schematic of a piezoelectric bimorph. Contraction of the bottom patch by applying a voltage causes the leaf-flexure to bend and the mass, m, to move upwards. This results in stretching of the top patch which can be used as a sensor to detect the movement.

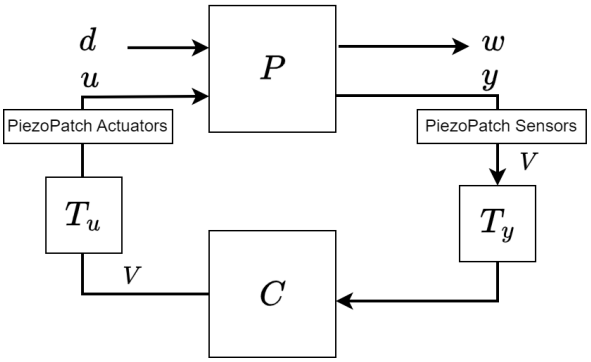

Figure 1.3: Block diagram of the proposed active vibration suppression scheme. Here the suspension mechanism is represented by the plant, P. The actuator inputs, applied via piezoelectric patches, are represented by u, the disturbance by d, the output position of the metrology frame by w, and the sensor reading by y. T_u and T_y are decoupling matrices. The controller, C, is to be designed such that the resonances of the first six mode-shapes in the transfer from disturbance to output are damped.

are to be used. The six resonances corresponding to the 6 DoFs of the frame in the transfer from disturbance, d, to output position of the metrology frame, w, have to be damped. This requires sufficient coupling from the inputs, u, to the output, w, and from the disturbance, d, to sensor output y. For this, it needs to be ensured that the mode shape of the vibration couples to a strain in the piezoelectric patch.

It is important to discuss why one would want to use the proposed method in this specific case, as there are a multitude of options to tackle the problem of attenuating parasitic vibrations. First of all, an option that could be considered is feeding forward the vibrations in the metrology frame to the controller of the short stroke stage, in order to follow the vibrations of the metrology frame. Such a solution can effectively decrease tracking errors, but is inherently limited by sensor noise and modelling accuracy. Another typical solution is to implement a Tuned Mass Damper (TMD) [3]. A TMD is typically placed at the point where the vibrational energy is highest, adding mass and volume at this point. This can conflict with the system design as this is often also where key functioning parts of the system are placed, such as optical elements. It may thus not always be possible to implement a TMD at the desired location. Additionally, it can be difficult to retrofit a TMD into a design if a parasitic resonance is discovered when testing the system. This is a key advantage of using piezoelectric patches. The patches can be applied retroactively at locations where there is high strain due to the mode shape of the vibrations. The active approach using patches also gives greater adaptability. Resonance frequencies can shift over time or position of the system, this can be accounted for by tuning the control parameters of the active vibration suppression algorithm. In the case of a TMD, a resonance shift would lead to decreased damping performance, or the TMD has to be adapted, requiring a change of hardware. All in all, it can be said that the active approach using piezoelectric patches provides a solution to suppress vibrations in cases where other solutions could not be feasible, or not desirable due to their lower adaptability.

The aim of this work is two-fold. First, we want to demonstrate and evaluate the achievable damping of the eigenfrequencies of a 6 degree of freedom suspended frame using piezoelectric patches as integrated sensor-actuator pairs. Secondly, to provide a framework of the design steps required to realise the suspended mechanism. Steps in this process include sensor/actuator placement to ensure sufficient coupling, system identification and structured parameter estimation, decoupling of the MIMO system and optimally tuning a PPF controller

for each mode. None of the individual techniques used in this work is newly developed, but the entire framework to achieve this does not exist, as far as the author is aware.

This report is structured into four main sections. Chapter 2 covers the design process of the mechanical setup that will serve as a demonstrator of this active vibration suppression mechanism. Chapter 3 covers the validation of the design after it has been assembled. Chapter 4 covers the decoupling and controller design. The performance results of the active vibration suppression are presented in chapter 5. Finally, the conclusion and recommendations are given in chapters 6 and 7.

2 Mechanical Design

2.1 Introduction

The following section concerns the mechanical design of the six degree of freedom (6-DoF) compliant mechanism which will be damped by piezoelectric patches. Looking back at Figure 1.3 the design challenge addressed in this chapter is summarized as follows: "Design the plant, P, such that a controller, C, can suppress vibrations at the frequencies of the nominal modes of P." There are more requirements on the designed mechanism, these are listed in the first subsection concerning the design specifications. Some background research on potential solutions is provided, before moving on to the concept designs and evaluation thereof. The remainder of this chapter concerns the chosen concept, and the steps taken to ensure the design specification are met, including the modelling, detailing, and pre-production validation.

2.2 Design Specification

The design specifications are listed in Table 2.1. Requirement 1 ensures that the demonstrator setup behaves analogous to comparable industrial systems. Requirement 3 is important as the bandwidth of the controller of the short-stroke stage is limited by the parasitic resonances present in the system. The parasitic resonances can lead to stability issues of the controller. The bandwidth of the short-stroke controller needs to be sufficiently high in order to ensure performance of the short-stroke. The fourth specification ensures the system is robust against accidental impacts or large disturbances, as it will also be taken to conventions, where the environment is not always controlled. Due to production and assembly tolerances, it is impossible to guarantee the exact position of the metrology frame, and sensors. Therefore, requirements 5 and 6 ensure suitable adjustability of the position after assembly, such that sensors can be brought into the correct range of the short stroke mechanism. The range of the capacitive sensors is 100 micron, thus a resolution of 10 micron is decided such that it can be ensured that the capacitive sensors can be positioned in the middle of the measuring range. Requirement 7 is a result of the approved financial budget for the assignment. Requirement 8 is based on an early estimate of the expected disturbance. A more thorough calculation of the minimum expected disturbance is presented in section 2.7. Requirements 2 and 9 are related to the specific aim of the demonstrator.

2.3 Literature Review

Compliant mechanisms are widely used in the precision industry due to their high repeatability, predictability, lack of back-lash and their maintenance free nature. Due to the high industrial relevance much research has been done on 6-DoF manipulators. In 2011, Dunning et al. published a review on the various designs of 6 DoF precision stages [4]. While the requirements of a precision stage and an isolation frame are different, the use of compliant elements in both systems will be similar. In compliant mechanisms motion is achieved through elastic deformation of so-called flexure elements, which is separated into two categories in the work of Dunnning et al. Lumped compliance refers to flexures where motion is achieved due to high stress concentrations around small and thin sections of the the flexure. An example of this kind of flexure are notched hinges. On the other hand, distributed compliance refers to flexures where the motion is achieved through the flexibility of the entire element, with a lack of stress concentrations. Typical examples are leaf and wire flexures. The distinction between the two is important in this work due to the use of piezoelectric patches. Typical sizes for piezoelectric patches are in the order of 50 mm $\times$ 50 mm $\times$ 0.2 mm. As a result piezoelectric patches cannot

Number	Requirement
1	The mechanical suspension needs to have 6 DoF, with eigenfrequencies between 10 Hz and 20 Hz.
2	Piezoelectric patches need to be used to achieve active vibration suppression of the compliant DoFs.
3	The eigenfrequencies of all higher modes beyond the first eigenmode per DoF, thus mode 7 and up, need to be greater than 200 Hz.
4	Stress limits of the flexures shall not be exceeded within the range of motion of the suspension. The range of motion of the suspension will be limited by end-stops.
5	The design needs to include the ability to adjust the distance between the metrology frame and short stroke. Required adjustability in z-direction: 40% of calculated deflection due to gravity. The minimum adjustability in x-y direction should be 0.5mm. The minimum adjustability in rotational direction should be 3 mRad.
6	The adjustability shall be possible with a resolution lower than 10 micron.
7	Production costs of frame + suspension need to be below 5000 euros.
8	The production lead time of the design should be approximately 10 weeks.
9	Vibrations with amplitudes in the order of 10^{-8} meters shall lead to measurable voltage changes on the piezoelectric patch used for sensing.

Table 2.1: The design specifications set-up at the beginning of the project.

be used with flexure elements with lumped compliance, as the patches can not be applied to the areas where the stresses and strains are highest. For this work, only designs making use of distributed compliance will be considered. Specifically, flexures of interest are leaf springs and folded leaf springs, as their form factors matches well with the use of piezoelectric patches. A leaf spring constrains three degrees of freedom (2 translations and 1 rotation), while a folded leaf spring constrains only translation in the direction of the fold line.

Dunning et al. found that a vast number of 6 DoF manipulators are parallel mechanisms, for example adaptations on the classic Stewart platform. This provides dynamical advantages at the cost of limiting the workspace of the manipulator. Examples are a MEMS based manipulator developed by Brouwer et al. in 2010 [2], or the hexablade positioner of Yang et al. [20]. In the first case comb drives are used to move the struts connected to the platform. In the latter case voice coils are used to actuate the position of folded leaf flexures which are used as the struts to control the platform. This kind of set-up has been proven to be able to achieve significant vibration attenuation in 2016 by Wang et al. [19]. While it is possible to design such a parallel mechanism actuated by piezoelectric patches, it does not offer significant advantages over the use of voice coils. Using this method to achieve the vibration suppression would nullify the industrial relevance of this work. As such, no concept will be generated where a parallel mechanism in this form is used.

In order to design a suspension mechanism using leaf- or folded leaf flexures, a serial stacking of parallel mechanisms is considered. As soon as one element is connected between the base and metrology frame, at least one translation is constrained by the flexure element [10]. The stacking in series is required to release this constraint such that the metrology frame has 6 degrees of freedom. A synthesis method for serial flexure mechanisms using Freedom and Constraint Topology (FACT) is described by Hopkins et al.(2011). A logical approach would be to stack two 3 DoF stages in series, one planar stage constraining out of plane movement and rotations, and one tip-tilt-piston (TTP) stage constraining any planar movement. The serial stacking of these stages releases all constraints from the ground to the metrology frame.

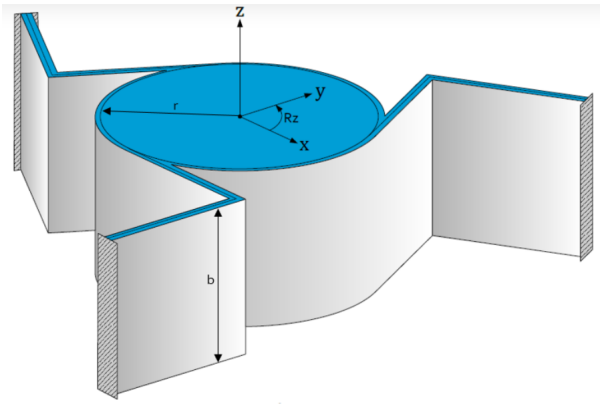

Figure 2.1: A planar stage consisting of three folded leaf flexures in parallel, constraining out of plane translation and rotations. Image from JPE [12].

In the textbook 'Design Principles for Precision Mechanisms' a frequently used planar stage is presented [17]. As can be seen in Figure 2.1, three folded leaf springs are placed in parallel to constrain all out of plane movements (vertical translations and rotations around the x- and y-axis). By rotating the folded leaf springs such that the fold lines lie in the same plane, a TTP stage is created. This could serve as a potential solution for the mechanical design.

Alternatively, it is possible to design a flexure element which is flexible in all 6 rigid body directions. By adding a second fold to a folded leaf flexure. This idea originated from the work of Lemmen et al. presented in [13]. This would eliminate the need for an intermediate body as required for serial stages and could thus be an interesting design path of which the potential needs to be explored.

2.4 Concept Evaluation and Selection

From the background research two main possible solution paths were identified and these are to be evaluated. A sketch of Concepts 1 and 2 is presented in Figure 2.2. Starting point for the designs are the required design dimensions of the metrology frame. This is pre-determined by the location of the sensors which measure the position of the short-stroke. This gives an initial mass of the suspended payload, meaning that geometrical parameters for the flexures can be determined. From there, design iteration is modelled using SPABS [14], which is an extended version of the multibody software SPACAR [11]. SPABS requires a much lower computational time in comparison with conventional volumetric-element based finite element solvers, making it ideal to use in an iterative design stage, as the effect of geometrical changes can be determined quickly in order to explore a design space. In this phase, it is important to keep into account that the frequency response of compliant suspension mechanisms can simply be modelled as a mass-spring system. In that case the eigenfrequency in a respective direction is given by Equation 2.1. Here, k is the total stiffness of all flexures for the considered direction, m is the suspended mass and f is the eigenfrequency. For the rotational modes, the mass is replaced by the moment of inertia, and k represents the rotational stiffness.

$$f = \frac{1}{2\pi}\sqrt{\frac{k}{m}} \tag{2.1}$$

A targeted eigenfrequency for a nominal mode or a parasitic mode can thus be achieved by changing the mass or the stiffness in the direction of the mode. For any given suspension

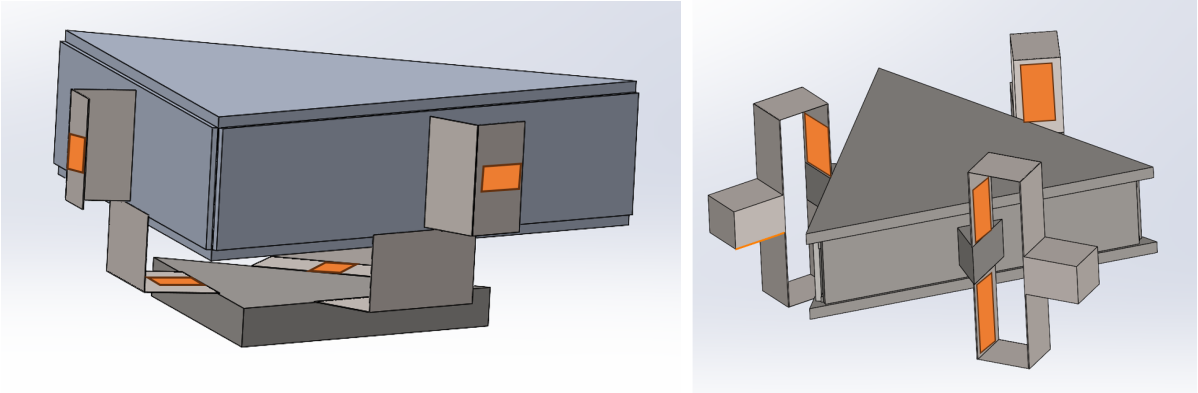

(a) Concept 1 **(b)** Concept 2

Figure 2.2: Sketches of the two concepts evaluated in the early phase of this project. The piezoelectric patch locations are marked in orange.

configuration, it is thus important to identify the parameters controlling the stiffness of the compliant mode and the parameters controlling the stiffness of the parasitic mode. This way, in the design phase a suspension mechanism with a desired low nominal frequency can be designed, while also guaranteeing high parasitic frequencies.

Helpful for the design exploration and iteration phase, SPABS provides a state-space model of the system, from which actuator to end-effector transfers can be determined. This allows us to evaluate if there is coupling between the six modes shapes to be damped and the actuators in the concepts.

As a side note, in concept generation phase more designs were synthesized than the two concepts that are evaluated below. However, these designs were disregarded in an earlier phase due to identified problems with those designs. As a consequence these designs will not be discussed in this work.

Concept 1

Concept 1 is a serial combination of two 3-DoF stages, each constrained by three leaf flexures arranged symmetrically. The intermediate body is free to move in all planar directions. The stiffness for the translation of the intermediate body is independent of the in-plane direction and is given by [17]

$$k_{xy} = \frac{45Ebt^3}{24L^3} \tag{2.2}$$

Parameters are the width of folded leaf spring along the direction of the fold, b, the thickness, t, and the length of the flexure L. On the other hand the out of plane stiffness of the intermediate body scales with tb^3, $k_z \sim \frac{tb^3}{L^3}$. Therefore to maximise the parasitic eigenfrequency while keeping the frequency of the nominal modes low, the ratio $\frac{b}{t}$ should be maximised, within reason. The same design rule of thumb holds for the second stage in the concept. Keeping this in mind, the design space was explored using SPACAR. The resulting system parameters and frequencies are presented in Table 2.2. Note that while only four low frequent eigenmodes are mentioned, due to the symmetry of the setup the modes for planar translations, and tip-tilt rotations are double modes.

Mass Metrology Frame	5.8 kg
Mass Intermediate Body	14.8 kg
Folded Leaf Dimensions - Planar Stage	$L = 70$mm, $t = 1$mm, $b = 130$mm
Folded Leaf Dimension - TTP Stage	$L = 60$mm, $t = 0.5$mm, $b = 130$mm
f_{xy}	14.8 Hz
f_z	11.3 Hz
$f_{\theta_x\theta_y}$	13.1 Hz
f_{θ_z}	17.8 Hz
First Parasitic Frequency	288 Hz

Table 2.2: System properties of concept 1.

Concept 2

Concept 2 utilises a flexure concept that constrains zero degrees of freedom. The concept is built up of out of leaf-flexures with 2 folds. As such, no intermediate body is needed to create a serial chain. A symmetric arrangement of these 6-DoF hinges was chosen. In this case, there are more parameters in the design that can be varied. The orientation of the hinges, has great effect on the coupling of the patches to various mode shapes. The length, L_2, in between the two folds can be varied as well as the length between the connected body and the first fold, L_1. However, due to the parallel nature of the structure, the change of one variable has impact on the frequencies of all mode shopes. It is therefore less intuitive to adjust parameters to reach the desired specification. The system parameters for this concept are presented in Table 2.3.

Mass Metrology Frame	10 kg
6-DoF Hinge Dimensions	$L_1 = 70$mm, $L_2 = 46$mm, $t = 1$mm, $b = 40$mm
f_{xy}	12.2 Hz
f_z	10.9 Hz
$f_{\theta_x\theta_y}$	19.9 Hz
f_{θ_z}	18.4 Hz
First Parasitic Frequency	204 Hz

Table 2.3: System properties of concept 2.

Concept Comparison

First of all, it is clear that both concepts can lead to a system with the desired frequency specifications. However, as can be deduced from Table 2.3, the design of concept 2 is only marginally within the specifications. This is noticeable in the frequencies of modes f_z and $f_{\theta_x\theta_y}$. The former is at the bottom of the desired frequency specification, while the latter is at the top of the desired frequency range. The most effective way to solve this would be to place the hinges closer to the center of the metrology frame, this is however not possible due to this being the space in which the sensors of the metrology frame have to be mounted. Other solutions would be to shift the mass of the metrology frame further to the outside, thereby increasing the moment of inertia. The extent to which this can be done is limited, as the rigidity of the metrology frame needs to be guaranteed. Additionally, the frequency will only shift with the inverse square root of the moment of inertia thereby requiring large mass shifts to achieve the desired effect. With more design time a more optimal solution for the parameters could have been found, but the fact remains that if later in the design phase adjustments to

bodies or geometries have to be made, it can become quite a challenge to ensure the design remains within the specifications. The more intuitive and separately tune-able modes in the serial mechanism of concept 1 can give an advantage if adjustments have to be made late in the design process.

The frequency response from position disturbances to position output is plotted in Figure 2.3 for both concepts. The most important difference that can be noticed from these plots, apart from the differing locations of nominal and parasitic resonances, is the high degree of coupling between rotational and translational modes for concept 1. This is due to the fact that the planar mechanism of concept 1 is mounted at the center of mass of the intermediate body. Ideally, it should be mounted at the center of mass of the intermediate body plus metrology frame. Now, vibrations in the x or y direction also generate a moment on the structure as a whole, leading to the stronger coupling to the rotational modes. This coupling is not visible for the responses of concept 2.

The coupling between the patches and the vibrations of the end-effector can be characterised by the transfer function from patch voltages to the output position. Figure 2.4 compares the frequency response of this transfer function between the two concepts, for two displacement outputs, x and θ_x. The results that can be concluded from these plots is that for both concepts there is sufficient coupling between the actuation voltages of the patches and the vibrations induced at the end-effector. We see a DC response of approximately 2×10^{-8} m/V for the translational DoFs. A signal with amplitude of 1 V will lead to vibrations of amplitude 0.02 micron. Patch transducers can handle voltages upwards of 200 Volts. Therefore, there is sufficient coupling between patches and the metrology frame to attenuate vibrations in the order of micrometers. The conclusion and results for the other modes not shown in Figure 2.4 are the same, and therefore omitted from the main report.

Clearly, both concepts show promise and could be suitable solutions for achieving the aim of this work. A key advantage of concept 1 over concept 2 is the higher flexibility it gives in dealing with design choices throughout the process. The serial construction seperates the suspension into two subsystems which can be tuned, and adapted mostly seperately from each other. It also means that, if in the assembled design certain frequencies are out of specfication, it is easier to make changes that bring these frequencies back into specification. In the case of complications in the timeline of the project it also provides the option to implement the vibration suppression only on one of the serial stages. Concept 1 thus seems a more practical design to work with, and will be the concept for which a detailed design will be created.

2.5 Design Details

The final detailed design is presented in Figure 2.5. In the following subsection design decisions and details of the finished design will be highlighted.

First of all, what can readily be noticed is that the majority of the design is achieved using laser cut pieces of aluminium and stainless-steel. This choice was made for two reasons. First of all, laser cut pieces are a lower cost solution in comparison to machined components, this is important for remaining within the allotted budget for the assignment. Second, the production lead time of laser cut pieces is typically much lower than for milled parts.

2.5.1 Folded Leaf Flexures

The folded leaf flexures will not be produced as a monolithic part for the above mentioned reasons. The folded leaf flexures will be assembled by clamping two laser-cut leaf flexures at 90 degree angle relative to each other, as illustrated in Figure 2.6. Care has to be taken that

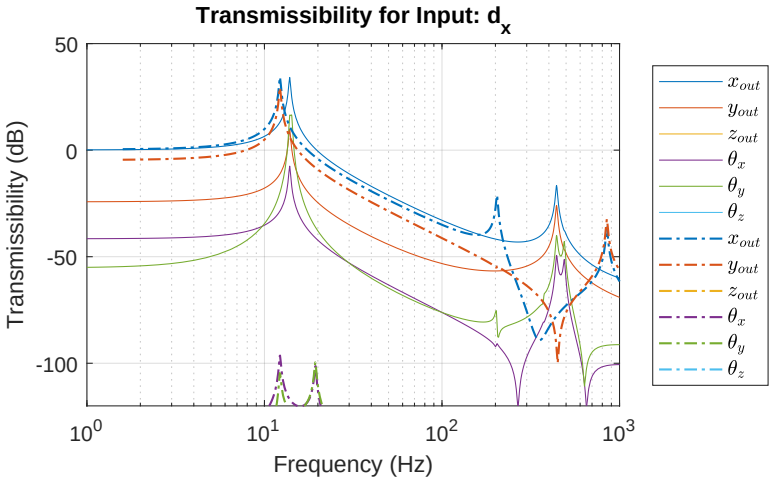

(a) Amplitude responses due to base disturbance in x-direction, d_x.

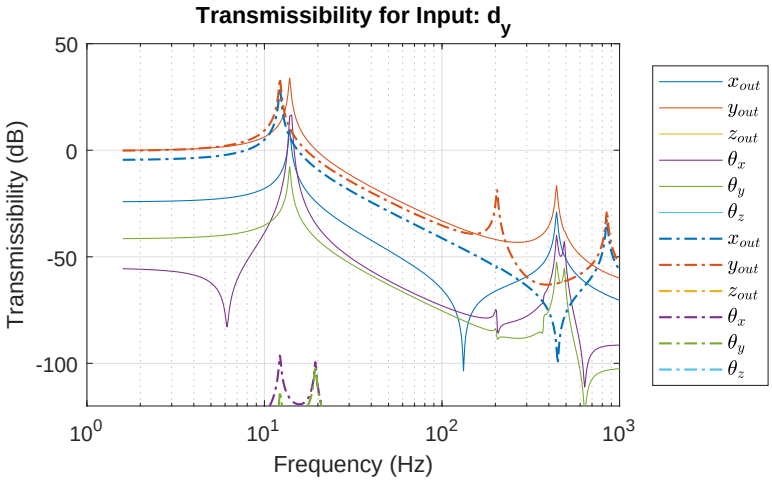

(b) Amplitude responses due to base disturbance in y-direction, d_y.

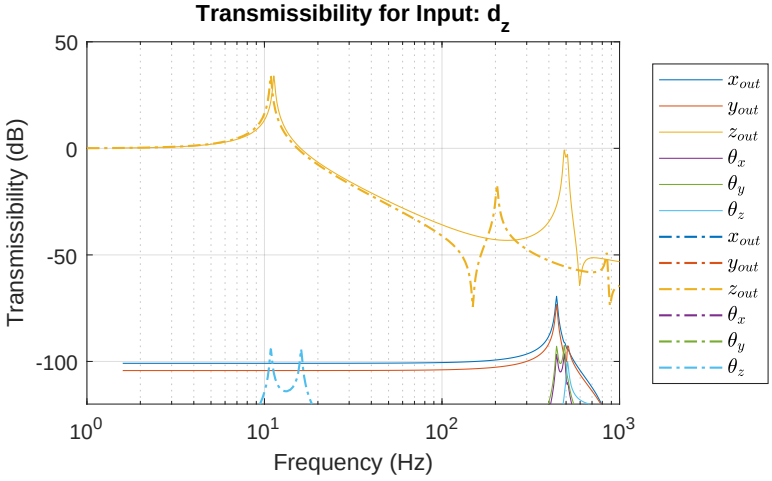

(c) Amplitude responses due to base disturbance in z-direction, d_z.

Figure 2.3: Amplitude responses for the transmission of disturbing floor vibrations to the output position of the end-effector. Concept 1 is given by solid lines, Concept 2 is plotted using dashed lines.

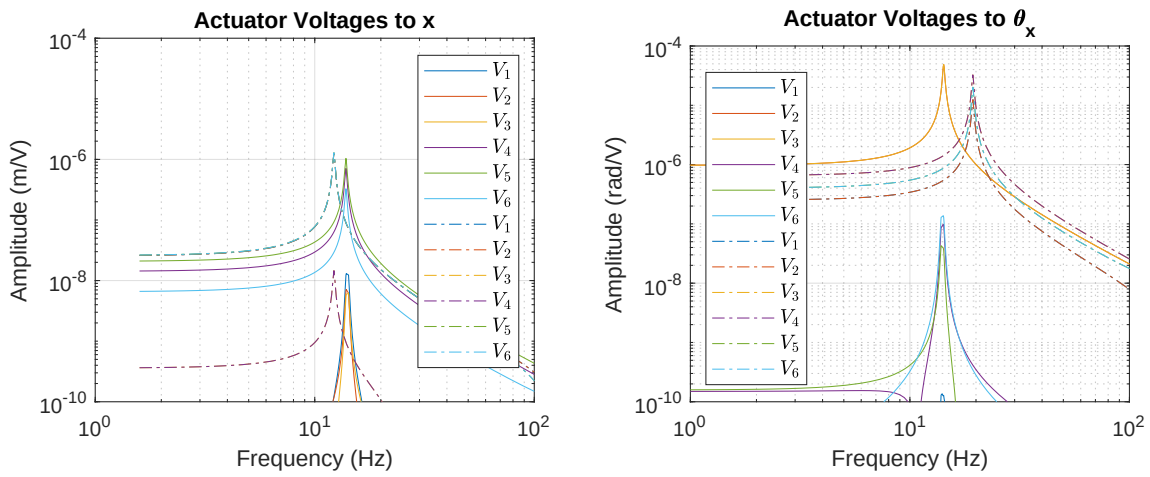

(a) Input voltages to x position of end-effector.

(b) Input voltages to θ_x position of end-effector.

Figure 2.4: Amplitude response of the transfer from patch voltages to the position of the end-effector for the 2 concepts. Solid line: Concept 1, Dashed Line: Concept 2.

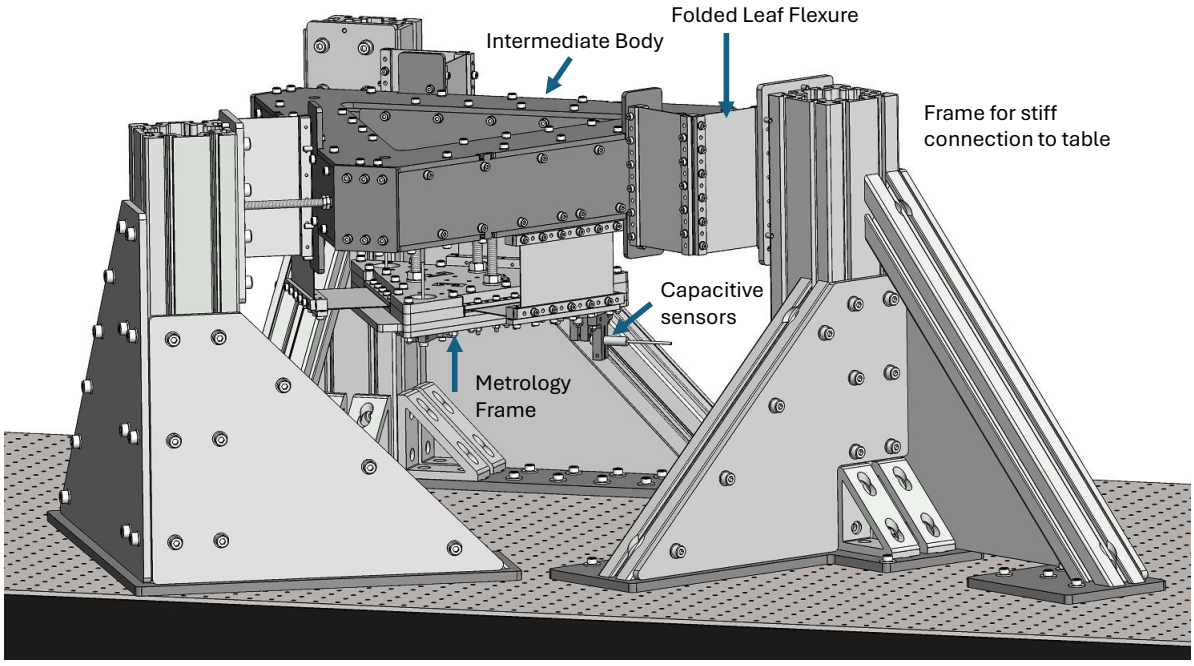

Figure 2.5: Overview of the final design. A short-stroke mechanism will be placed below the metrology frame.

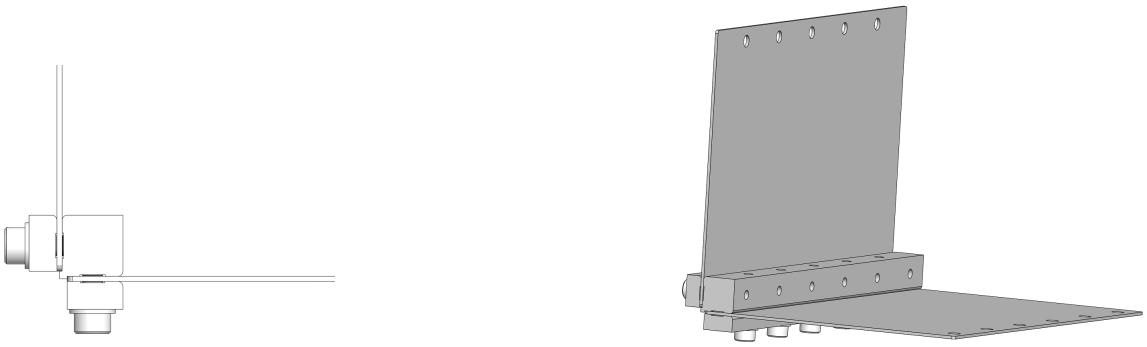

(a) Side view **(b)** Isometric view

Figure 2.6: Folded leaf flexures created by clamping of two leaf flexures.

the position of the leaf flexure in the clamped connection is well defined. As such a backstop is created against which the leaf flexure is positioned. On the other edge the leaf spring is designed to be perfectly flush with the clamping block. Clamping jaws create a smaller defined surface to which the leaf spring is clamped. This ensures a high clamping pressure, and reduces hysteresis effects in the clamped joint due to micro-slip [17]. The material from which the leaf flexures are produced is AISI 301. This stainless steel is utilised for its relatively high tensile strength. The clamping parts have to be produced by milling, but because a high number of these parts is required the price per unit is relatively low. This is because the start-up costs will only have to be payed once, and these are often the cost-drivers for milled components.

2.5.2 Positioning of assembled parts

A design challenge due to the use of laser-cut pieces is ensuring that all parts are positioned as exactly as possible. The laser-cut pieces will be joined together using bolt-nut combinations. For this clearance holes are used, which are typically 0.6mm to 1mm larger in diameter than the bolt. This creates a large range within which pieces can be assembled. This is undesirable. To solve this problem clear points of contact are implemented that constrain the parts relative to each other. Two examples of how this is done are shown in Figure 2.7. Figure 2.7a shows the use of spring-type straight pins, which protrude from the surface in order to create three defined contact points. The spring-type straight pins adapt their size to the hole in the laser-cut part, therefore no tight tolerance requirement is needed for the hole size, which saves in costs. In Figure 2.7b the three contact points are defined by laser-cut tabs in the geometry. These two methods are mainly used to ensure well defined positioning of the to be assembled parts. This does not ensure positional accuracy, as there are still production tolerances on the manufactured pieces. For laser-cut pieces these tolerances will be in the range of 0.15 to 0.6 mm depending on plate thickness and feature size. With multiple pieces positioned in series, these tolerances can accumulate throughout the design, and lead to positional inaccuracies. This is why it is a necessity to have the option to make adjustments to positioning of the suspension.

2.5.3 Adjustment mechanisms

In the design there are three methods with which the position of either the capacitive sensors, or the metrology frame as a whole can be adjusted, relative to the short-stroke. First of all, the capacitive sensors can be moved forwards or backwards within their clamps. The capactive sensors have a measuring range of 0.1mm and need to be placed at 0.25mm from the

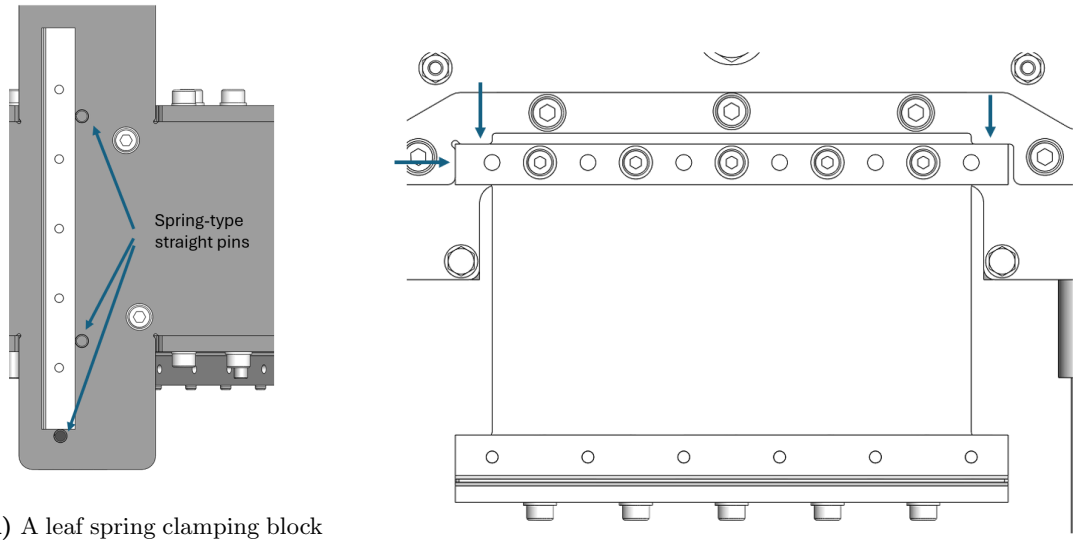

(a) A leaf spring clamping block is positioned on top of the intermediate body side-wall using three spring-type straight pins as contact points.

(b) Three clear contact points have been defined by the blue arrows for positioning a clamping block within the same plane of a part of the metrology frame.

Figure 2.7: Two methods to clearly define the position of two parts before joining them together.

measurement plate to be in the middle of their sensing range. Releasing the clamping bolt, can allow the sensor body to be slid closer or further, with continous and fine adjustment to place the sensors in the correct range. Note that these clamps, were not designed as a part of this work, and were already in use in the pre-existing set-up for the short stroke.

The clamps cannot be used to adjust the angle of the sensors if the sensors' surfaces are not parallel to the measurement surface. In this case, the planar position and rotation of the entire short-stroke mechanism can be moved using three turnbuckles, as depicted in Figure 2.8a. The turnbuckles provide 2mm of adjustment in x and y direction, and allow for angular adjustment in θ_z of $\pm 1°$.

The height, and tip-tilt angles (θ_x, θ_y) of the metrology frame can also be adjusted. This is done by changing the height at which the entire suspension mechanism is mounted to the uprights of the supporting frame. Contact between a spring-type straight pin and the top surface of the upright determines the mounting height, as illustrated in Figure 2.8b. Shims can be placed in between this contact point to increase the height. By only adjusting the height of one of the mounts the tip-tilt angles can be adjusted accordingly. The ordered shim plates allow the total height of the mechanism to be adjusted up to 1 mm, in steps of 0.1 mm.

2.5.4 End stops

End-stops are implemented to limit the movement of the bodies to within the stress limits of the flexures. The implementation of the end-stops is shown in Figure 2.9. The maximum deflection will be calculated for the z-direction because due to gravity these flexures will be loaded the most. As movement between intermediate body and the end-effector is constrained in the xy-direction, it can be argued that a single folded leaf flexure can be modelled as a guided folded leaf-flexure. The maximum stress, σ_{max}, in a guided leaf flexure is given by [17]

$$\sigma_{max} = \frac{9}{4}\frac{Etu_z}{l^2} \tag{2.3}$$

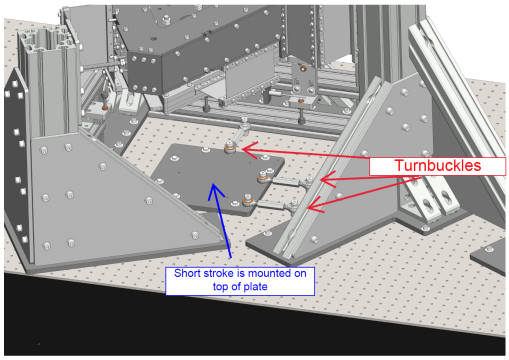

(a) Three turnbuckles connected to the base plate upon which the short stroke is mounted. Adjusting the turnbuckles allows the rotation and position to be modified.

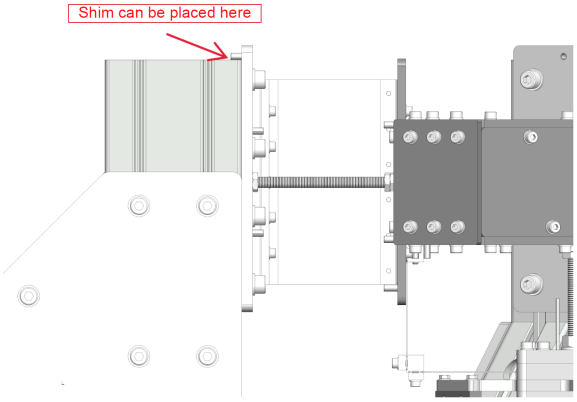

(b) The height and tip-tilt angles θ_x and θ_y can be adjusted by placing shims between the pin and the top surface of the frame uprights.

Figure 2.8: The available methods for adjusting the relative position of the short-stroke and metrology frame.

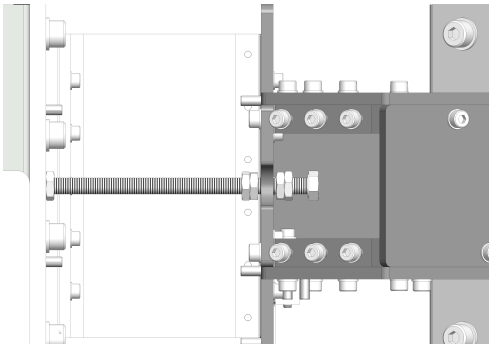

(a) Implementation of end-stops limiting the movement of the intermediate body.

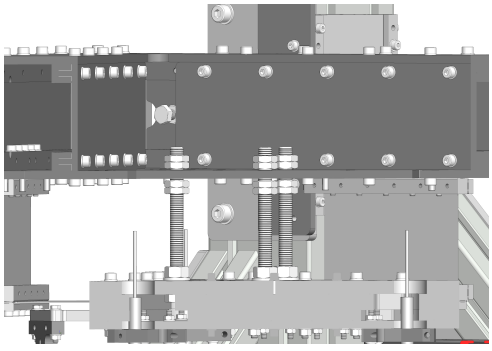

(b) Implementation of end-stops limiting the movement of the end-effector

Figure 2.9: The implementation of end-stops to constrain the movement of the metrology frame to within the stress limits of the leaf flexures.

Here E is the elasticity modulus, t is the thickness, l the length of each leaf flexure, and u_z is the displacement in z-direction. The yield strength of AISI 301 is atleast 276 MPa. Assuming a safety factor of 2, to account for possible pre-tension in the finished assembly due to misalignment, the maximum deflection is then given by:

$$u_z = \frac{\sigma_{\text{yield}}}{2} \frac{4l^2}{9Et} \tag{2.4}$$

Using $E = 190\text{GPa}$, $l = 70\text{mm}$, $t = 0.8\text{mm}$, we get a maximum deflection of $u_z = 1.9\text{mm}$. We have to take into account the deflection due to gravity of the mechanism. This can be derived by requiring force balance:

$$k_z u_z = mg \tag{2.5}$$

$$k_z = \frac{mg}{u_z} \tag{2.6}$$

Substituting this into Equation 2.1 and rearranging we have

$$u_z = \frac{g}{4\pi^2 f_z^2} \tag{2.7}$$

We can conclude that for a suspension frequency of 13.5 Hz that the deflection due to gravity will be 1.4mm. Therefore the end-stops will be placed at $\pm 0.5\text{mm}$ to limit any further movement to within the stress limits of the flexures.

2.5.5 Patch placement

The location of the patches on the folded leaf flexure is important in determining the electro-mechanical coupling. If for instance in Figure 1.2, the top patch was not placed at the end of the flexure but in the middle of the flexure there would be little coupling. This is because at the middle of the flexure the strain changes sign, going from compressive to tensile strain, as one moves from the left side of the flexure to the right side. If one side of the patch is compressed, and the other half stretched the net result is that the charge movement within the material is cancelled out, leaving no measurable signal. It is clear then, that the patches have to be located at the ends of the leaf-flexures where the stresses are highest. The mode shapes of the system are displayed in Figure 2.10. For each mode shape the stresses on the patches are plotted using color coding. In dark blue are low stress regions and in yellow/orange are high stress regions. First looking at modes 1,2, and 3, we see that the placement of the patches is mostly dictated by mode shape 3. For modes 1,2 the patches could be placed on the flexure as close as possible to the clamping point on the frame. This will give slightly better coupling than the location depcited in Figure 2.10. However, for mode 3, stresses are by far highest near the intermediate body, giving significantly better coupling for that mode. This is the main reason, the patches were placed as close to the intermediate body as possible. For modes 4, 5 and 6 there are were 2 plausible positions. On the lowest flexure at the closest point to the end-effector, or the other flexure as close to the fold as possible. No significant difference in coupling between those 2 locations was found. It was therefore decided to place the patches as close to the metrology frame as possible, as this is a more practical location to manage the wiring of the assembly.

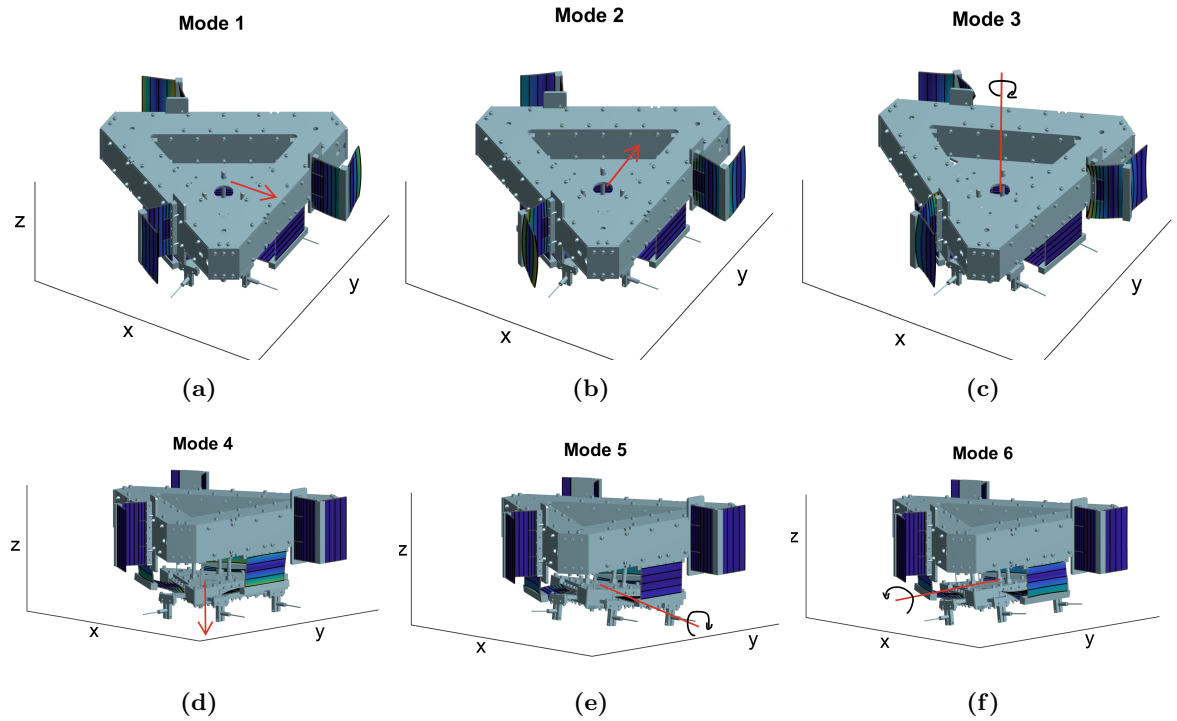

Figure 2.10: Visualisation of the 6 nominal mode shapes of the system. Regions of high von Mises stress are yellow, and low stress dark blue.

2.6 Pre-production Design Validation

Before moving to production and assembly of the design it is important to perform a validation using finite element analysis (FEA) to ensure the system will behave as expected. The main reason that this is important, is because in the modelling within SPACAR, the intermediate body, and metrology frame are assumed to be rigid bodies. In reality, these will also have some flexibility. The flexibility of these bodies can lead to lower parasitic frequencies than expected. Furthermore, a FEA is also required of the outside frame supporting the mechanism in order to ensure that it also has a high enough stiffness. Ansys Mechanical is used to carry out a modal analysis of the designed suspension mechanism.

In order to run a FEA of the design, first the design has to simplified, removing all holes and bolts, and only keeping the general geometric shapes and dimensions in the form of monolithic parts. This is necessary in order to reduce the amount of elements and nodes required to generate a representative finite element mesh. This keeps the computational effort required maneagable and allows the FEA to be performed using a laptop. Figure 2.11 shows the used mesh and geometry for the FEA. A sweep method, where a face of a body is meshed and subsequently swept through the whole body, has been employed in order to mesh the leaf springs. This creates a structured mesh, which requires a lower node count to obtain accurate results compared to a random mesh. Additionally, in order to be able to accurately to model the stresses within the leaf spring, it is ensured that there are two elements over the thickness of the leaf spring. This is necessary because the strains will be opposite on opposing sides of the leaf springs, with two elements of thickness this can be modelled more accurately.

In order to determine whether the mesh is fine enough, multiple runs are done with each run increasing the mesh density. The results should be converging. This can be seen in Table 2.4. The frequency values for the modes related to compliance in the folded leaf flexures are

well converged. Mode 7 and 8 are not yet fully converged, however no finer mesh could be implemented due to the computational limits of the laptop.

From the results of the FEA it can be seen that due to additional compliance in the intermediate body, the first parasitic modes are at a lower frequency than expected using SPACAR. This result was expected. In fact, in the physical system these parasitic resonances might be positioned even lower, as in the FEA perfect contact is assumed between the different bodies. In reality this will not be the case, and this can often lead to lower parasitic frequencies than modelled. The nominal modes from the FEA are slightly lower than predicted from SPACAR. This can be explained by the fact that due to the simplification of the geometry, the total mass and moments of inertia of the bodies are no lower in the FEA simulation than the properties used for SPACAR.

To evaluate the stiffness of the supporting frame around the suspension mechanism another set up has to be made. For this case the suspension mechanism is modelled as a point mass with a known mass and moment of inertia. This point mass is connected to the 3 uprights of the supporting frame. This is done, because the computational resources required to model the suspension mechanism and the supporting frame simultaneously are too large. The aluminium extrusion frame pieces are meshed with a fine mesh in order to get representative results. The resulting first eigenmode of the support frame was found to be 320 Hz. This is sufficient to meet the parasitic frequency specification, but this number should be treated as a ball park figure. Due to the complicated meshing of the parts in the frame, no convergence study could be done and thus it is highly possible the solution is not yet fully converged. Thus a lower frequency can be expected from the support frame, but it is not expected that the supporting frame has a first eigenmode below 200 Hz. The supporting frame can therefore be considered stiff enough for the application.

Node Count	f_x	f_y	f_{θ_z}	f_z	f_{θ_y}	f_{θ_x}	**Mode 7**	**Mode 8**
273000	10.321	10.322	12.197	13.225	18.845	18.846	246.05	251.05
350000	10.335	10.355	12.212	13.237	18.856	18.858	251.91	253.19
1000000	10.327	10.327	12.2	13.257	18.879	18.879	242.87	248.11
SPACAR	11.6	11.6	13.1	14.3	18.5	19.1	266	266

Table 2.4: The resulting frequencies of the first 8 mode shapes from a modal analysis for different node counts.

2.7 Electrical Components

As for any mechatronic system it is important to consider the required electrical components in order to be able to perform the control objective. The sensor to actuator chain of components is shown in Figure 2.12. A surface charge is induced on the piezoelectric patches. A charge amplifier is used to convert the generated charge into a measurable voltage signal between -10V and 10V. The data acquisition (DAQ) is done using a PCIe card installed in a PC, which performs the analog to digital conversion of the signal. The digital signal is then used by the controller on the PC to calculate the required actuator voltages. Via the DAQ card an analog signal is generated, which is conditioned by the output voltage amplifier. The amplified signal then drives the actuator patches, which should, with a well tuned controller, damp the resonances of the system. In this section the considerations taken for the selection of each electrical component will be discussed.

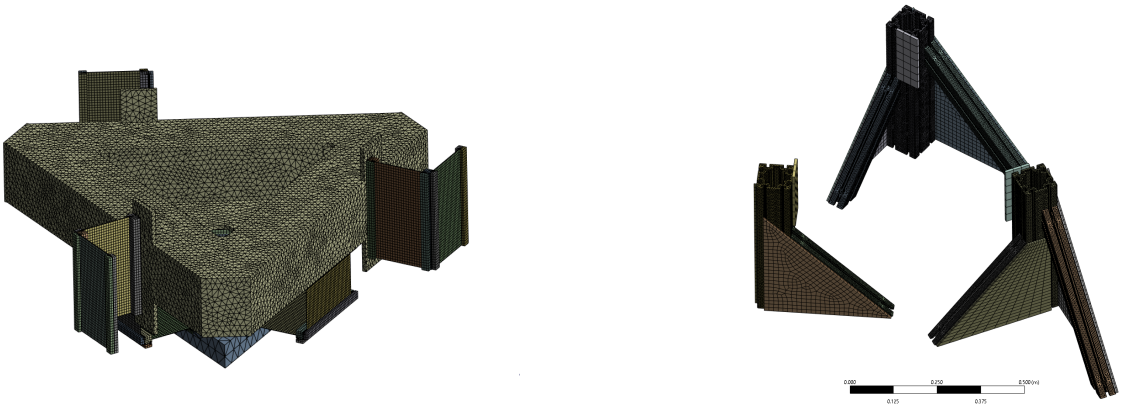

(a) Mesh of the suspension mechanism. **(b)** Mesh of the supporting frame.

Figure 2.11: The meshed geometries used for the finite element analysis of the supension mechanism and the supporting frame.

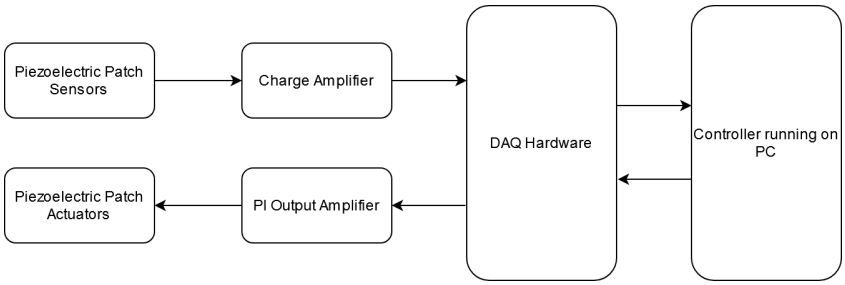

Figure 2.12: Diagram showing the required electrical components in order to implement the control task.

Piezoelectric Patches

The selected piezoelectric patches are PI DuraAct Patch Transducers P-876.A11. They have an operating voltage range -50V to 200V. The decision for these patches was made early on in the design process. This patch is flexible, robust and inexpensive, which suits the design specifications well. Also, we already established in section 2.4 that this patch will provide sufficient coupling to actuating the end-effector.

Control System and DAQ Hardware

The control system is implemented on a PC using Simulink Desktop Real-time. This setup was already being used for the short-stroke stage and therefore also has to be used for the piezodamping mechanism. PCIe cards from National Insturments (NI) are already being used in this PC for reading out the capacitive sensors, and actuation of the short stroke stage. The setup still had 2 free analog output ports, but a total of 6 are needed, one for each piezoelectric patch. This means an additional PCIe card with 4 analog output ports needed to be selected. Another factor in DAQ selection is ensuring a high enough input and output sampling rate can be achieved. A rule of thumb in controller design is to have a sampling rate of 20 times the bandwidth of the controller. This minimises the impact of delay on the system. The bandwidth of a PPF controller is in the same frequency range as the resonance to be suppressed. Since the resonances will be placed at 10-20 Hz, and taking a factor of safety of 2, a control bandwidth of 40 Hz is assumed to be required. This gives a minimum desired sampling rate of 800 Hz. The NI PCIe 6323 card was selected, as this card provides the 4 analog outputs, and can sample 12 channels at a frequency of 20 kHz, which is more than sufficient.

Charge Amplifier

A charge amplifier converts the generated surface charge on the patches to a voltage output. The used charge amplifier is a custom design made by Boi Okken en Bram Seinhorst, and is produced and assembled by Eurocircuits. One PCB provides four measurement channels. The charge amplifier gain selection is important, as we need to ensure a measurable signal is obtained. Concretely, the PCIe card can measure signals in a maximum range of ± 10V. The gain, G, of the charge amplifier is given by:

$$G = -\frac{1}{C_{fb}} = \frac{V_{\text{out}}}{q_{\text{in}}} \tag{2.8}$$

Here C_{fb} is the capacitance of a capacitor placed in a feedback loop from an op-amp within the amplifier circuitry. V_{out} and q_{in} are the output voltage and input charge, respectively. In order to choose C_{fb} accordingly, we need an estimate of the expected charge produced due to movements of the end-effector. Using SPACAR the charge output of the patches can be determined for a given vibrational amplitude.

A baseline for the expected vibrational amplitude can be determined from considering the disturbance created due to floor vibrations. From prior measurements of floor vibrations at the DEMCON offices, it was found that the vibrations conform to the VC-D vibration criterion. This stipulates that the rms velocity of floor vibrations as measured in 1/3 octave frequency bands is smaller than or equal to 6.25 μm/s. The velocity frequency spectrum can be converted to position by multiplying with an integrator $\frac{1}{s}$. The floor vibrations will first be attenuated by the optical table, and subsequently by the metrology frame suspension. The transfer function of floor vibrations to the tabletop, $H(f)$, is known as it is specified by the manufacturer. The

transfer from table to end-effector, $P(f)$, is extracted from SPACAR. The frequency spectrum of the position of the end-effector, $X(f)$, as disturbed by floor vibrations, V(f), is then given by:

$$X(f) = \frac{P(f)H(f)V(f)}{2\pi f} \tag{2.9}$$

Parseval's theorem stipulates that the total energy of a signal in time domain is equal to to the total energy of the signal in frequency domain. In other words:

$$x_{rms}^2 = \int_{-\infty}^{\infty} x(t)^2 dt = \int_{-\infty}^{\infty} X(f)^2 df \tag{2.10}$$

Using the above equation, the rms amplitude of the displacement vibration in 1 direction was estimated to be $x_{rms} = 33.4$ nm. This is the minimum expected vibration size. With the assumption that disturbances created to evaluate and showcase the controller would be larger, the decision was made to aim for a voltage signal between ±1V for vibrations of 200 nm. This seemed a good balance, giving room to measure larger and smaller vibrations. This is because the measurement range of the DAQ can be specified to be ±0.2V, ±1V, ±5V or ±10V, all ranges measured with 16-bit resolution. Meaning that vibrations amplitudes of 40 nm up to 2μ m can be measured with full resolution. For a displacement of 200 nm, a charge build up on the patches of around 1 nC was found. Using Equation 2.8, the required capacitor then has a capacitace of 1 nF.

In the circuitry, a resistor R is placed in parallel with the feedback capacitor. This forms a high-pass filter with a cut off frequency f_c of

$$f_c = \frac{1}{2\pi R C_{fb}} \tag{2.11}$$

For optimal signal to noise ration we want to ensure that the high-pass filter does not attenuate measurements above 10 Hz. It is thus desired to place the cut-off frequency at 1 Hz or lower. This requires, $R \geq 160M\Omega$. A resistor of 250 MΩ was selected, placing the cut off frequency at 0.64 Hz.

Output Amplifier

The output amplifier is a voltage amplifier with a gain of 25. The amplifier, PI E-835, is designed to work with the piezoelectric patches. It has a bandwidth of 4 kHz, which is more than sufficient for our application. The amplifier takes an input signal between -4V and 10V and amplifies it to between -100V to 250V. Therefore to protect the patches, we need to limit the input signal to between -2V and 8V, which is possible to do in software. Each amplifier has one channel only, therefore 6 amplifiers are needed in total.

2.8 Design Summary

Throughout this chapter all considerations in the design process have been discussed. In this section we will review the specifications to see if the final design complies with them.

1. **The mechanical suspension needs to have 6 DoF, with eigenfrequencies between 10 Hz and 20 Hz.**

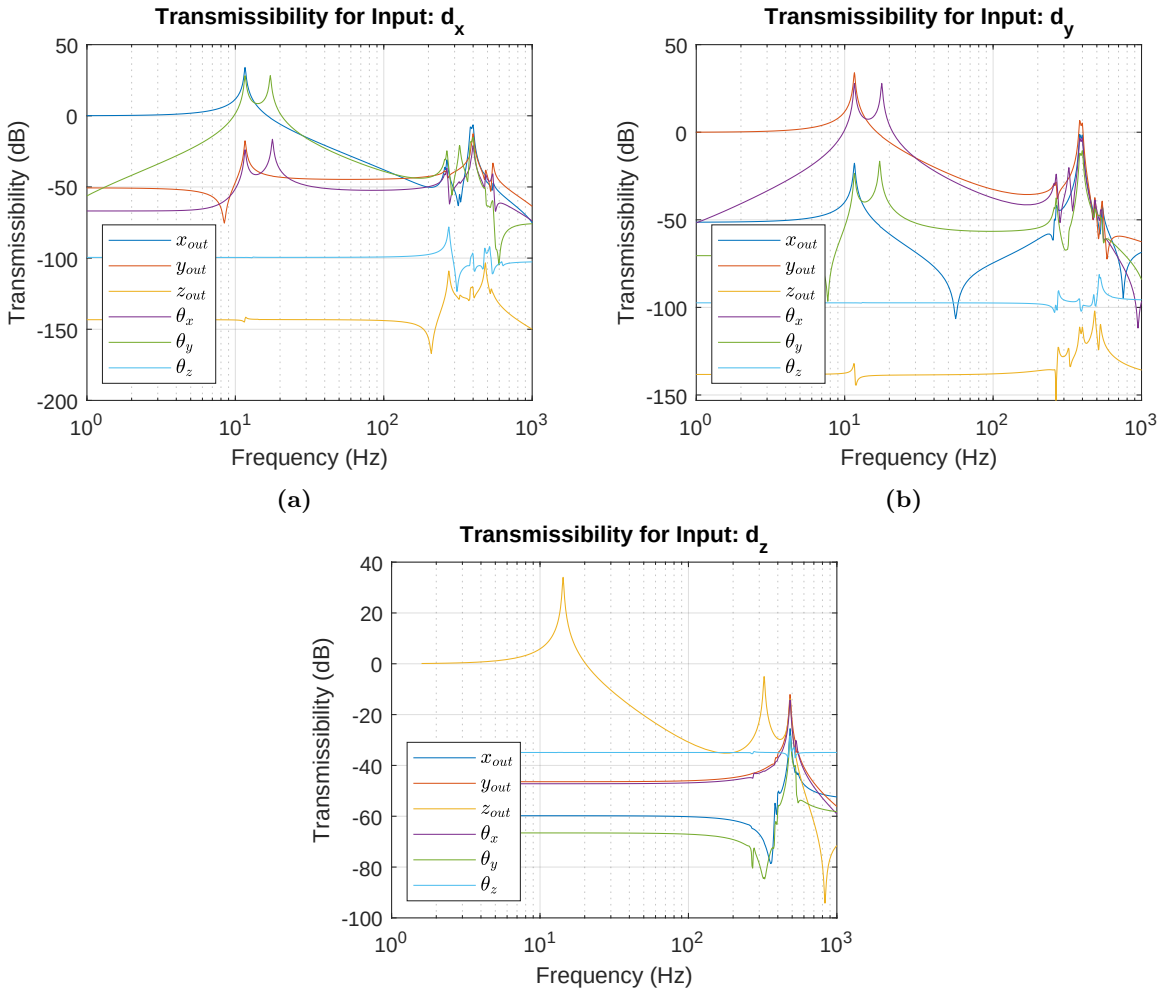

Figure 2.13: Amplitude responses for the transmission of disturbing floor vibrations $d = (d_x, d_y, d_z)^T$ to the output position of the end-effector, $w = (x, y, z, \theta_x, \theta_y, \theta_z)$.

The design has 6 nominal eigenmodes that are depicted in Figure 2.10. The eigenfrequencies of these modes were calculated using SPACAR and conventional FEA. The calculated eigenfrequencies are given in the bottom two rows of Table 2.4. As designed, all nominal modes lie between 10 - 20 Hz. The modelled transmissibility from base position disturbance to output position of the end-effector is shown in Figure 2.13. This highlights that the design indeed behaves as a suspension mechanism, where we see a second order roll-off of the transmissibility after the nominal eigenfrequency.

2. **Piezoelectric patches need to be used to achieve active vibration suppression of the compliant DoFs.**

We have ensured to integrate the piezoelectric patches at the points on the flexures subjected to the highest amount of stress, in order to maximise the electro-mechanical coupling. Figure 2.14 plots the transfers from patch voltages, to the position of the end-effector. For each nominal translational direction we see a DC amplitude larger than 0.04μm/V. As the operating range of a patch lies between $-50V$ to $200V$, this should be sufficient to attenuate vibrations in micrometer range.

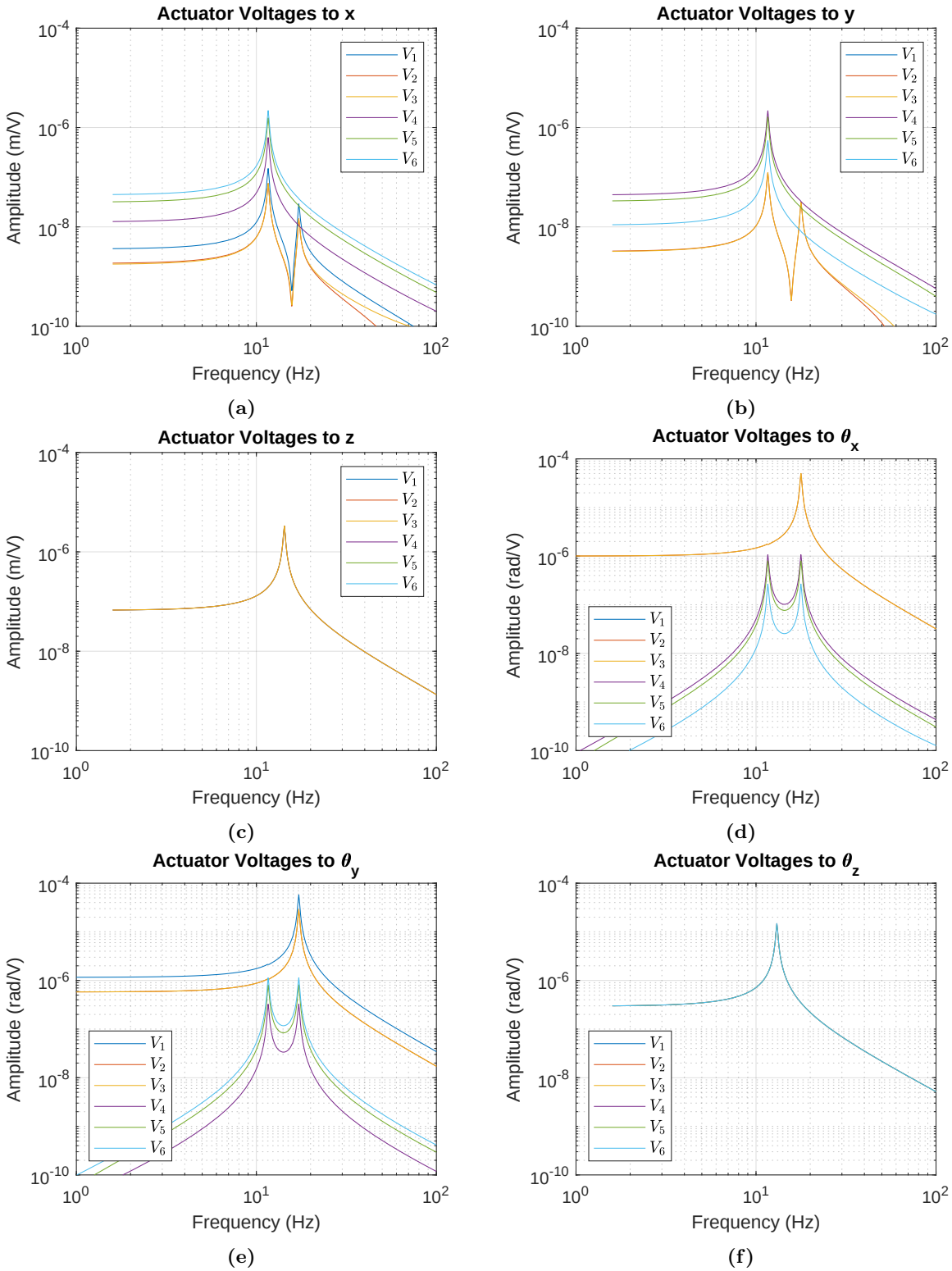

Figure 2.14: Transfer of actuator patch voltages $u = (V_1, V_2, V_3, V_4, V_5, V_6)^T$ to the output position of the end-effector, $w = (x, y, z, \theta_x, \theta_y, \theta_z)^T$.

3. **The eigenfrequency of all higher modes (mode 7 and up) needs to be greater than 200 Hz.**

A finite element analysis of the supporting frame, intermediate body and end-effector have been performed. The lowest parasitic mode was found to be 243 Hz. Note that we do expect the first parasitic mode in the finished assembly to be slightly lower than this, as underlying assumptions lead typically to stiffer models than in reality.

4. **Stress limits of the flexures shall not be exceeded within the range of motion of the suspension. The range of motion of the suspension will be limited by end-stops. This should make it impossible for the flexures to break or deform plastically due to accidental impacts.**

We showed using an analytical calculation that if the end-stops are placed at ± 0.5mm of the deflected position under gravity, then the stress in the flexure elements will not exceed the yield strength of the material. AISI 301 was selected as a material for the flexure elements due to its high strength characteristics in comparison to other stainless steels, helping to increase the robustness of the design.

5. **The design needs to include the ability to adjust the distance between the metrology frame and short stroke. Required adjustability in z-direction: 40% of calculated deflection due to gravity. The minimum adjustability in x-y direction should be 0.5mm. The minimum adjustability in rotational direction should be 3 mRad.**

6. **The adjustability shall be possible with a resolution of at least 10 micron. The range of the capacitive sensors is 100 micron. This way the mechanism can be adjusted to sit in the middle of the range of the capacitive sensors.**

The designed adjustment mechanisms provide a range of ± 1mm in xyz-directions. The angular adjustment is $\pm 1^\circ = \pm 17$mrad. The position of the capacitive sensors can be adjusted through a continuous range, hence they can always be placed within the center of the measurement range.

7. **Production costs of frame + suspension need to be below 5000 euros.**

Throughout the design phase much effort has been placed in ensuring the total package is as cost-effective as possible. Most parts are lasercut or catalogue parts. Milled parts such as the folded leaf-clamping parts, were standardized such that for both stages the same clamping parts could be used. The end-result is that the production costs for the mechanical construction was just below 5000 euros.

8. **The production lead time of the design should be approximately 10 weeks.**

Parts with longer lead-times were ordered early on in the design phase, these were for instance the piezoelectric patches and amplifiers from PI. The custom designed mechanical parts had a lead time of 2-3 weeks for laser-cut parts and approximately 5 weeks for the milled components.

9. **Vibrations with amplitudes in the order of 10^{-8} meters shall lead to measurable voltage changes on the piezoelectric patch used for sensing**

The gain of the charge amplifier has been chosen such that we expect an output signal of 1V for vibration amplitudes of around 200 nm. Meaning a signal of ± 0.2V for vibrations of order size 4×10^{-8}m. The 16-bit resolution of the DAQ hardware measuring over a total range of 20V provides a measurement resolution of 0.3 mV. Therefore, vibrations in the order of 10^{-8} meters can be measured.

To conclude, taking into account the above considerations and calculations, we expect the final design to meet all design specifications, and to provide a successful platform for demonstrating the potential of piezoelectric damping, in an industrially relevant setting.

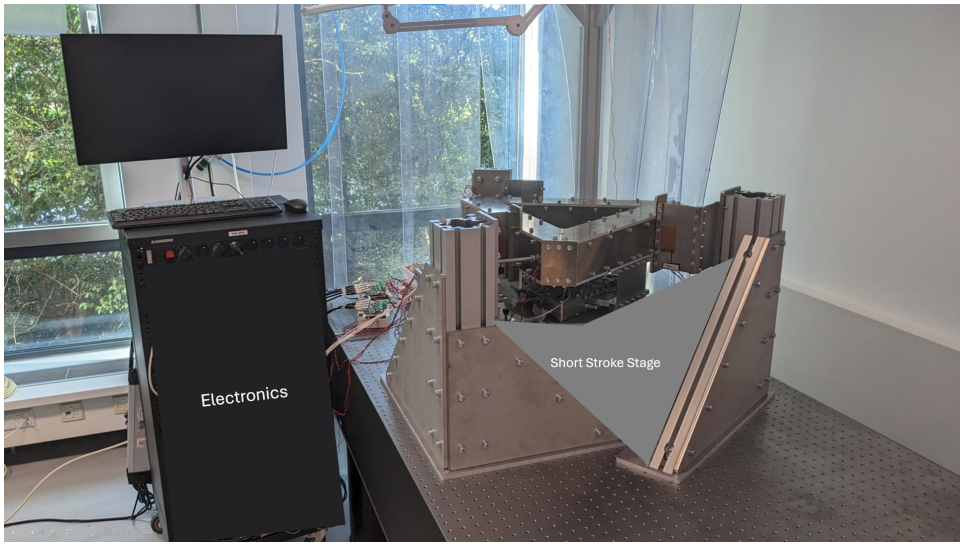

Figure 3.1: The final finished assembly.

3 Mechanical Design Validation

3.1 Introduction

In this chapter, system identification of the assembly is performed and compared to the dynamic model obtained from SPACAR. The nominal eigenfrequencies and associated mode shapes are determined, and the parasitic eigenfrequencies are identified. This serves to validate whether the finished assembly complies with the design targets, as well as being a necessary step before designing and tuning the controller. An image of the final assembly can be seen in Figure 3.1.

3.2 Methodology

3.2.1 Obtaining the Frequency Response of the System

In order to compare the assembly to the dynamic model, measurements of the frequency responses from input to output are desired. Specifically we are interested in the transfer from u to w, and the transfer from u to y. This can be achieved using Fourier analysis on time-domain measurements of the system response to a generated input signal. There are a few points that have to be taken into account, in order to obtain meaningful frequency response data. These points, such as windowing and used input signal, are discussed briefly in this section.

Since the system is linear, only frequencies present in the input signal will be present at the output. Therefore, it is important to generate an input signal that excites the system at the frequency range of interest. The input signal used is a white noise signal, which is injected into the system by the piezoelectric patches. White noise signals have a flat frequency spectrum, exciting all frequencies of the system equally.

The impact of measurement noise and disturbances can negatively impact the quality of the obtained frequency spectrum. In order to minimise the impact of noise, the frequency response is computed and averaged over multiple subrecords of data. Due to the random nature of the noise, averaging over multiple subrecords should reduce the impact of noise on the results. In this work the response is averaged over 20 subrecords.

The use of a white-noise input and subrecords of data will affect the measurement results by introducing spectral leakage. Spectral leakage occurs because the processed signals are not

periodic, while the Discrete Fourier transform (DFT) assumes that they are. To reconstruct the discontinuity at the start and end of signals, sinusoids with frequencies over the entire frequency domain are required. Thus, in the frequency domain, components will show up that are not present in the underlying signal, but are artifacts from the DFT method. To address this problem, windowing functions are used, where the Hann window and Hamming window are typical choices [1]. In this case the Hamming window is used. The Hamming window gradually attenuates the endpoints of the signal to near 0, reducing the discontinuity causing leakage over the entire frequency domain. The trade-off to using the Hamming window, instead of a rectangular window (or no window), is that it will lead to lower and wider resonance peaks in the frequency response. As such, it can limit the ability to distinguish between two closely placed resonances. The attenuation of the signal near the end-points leads to a loss of data in the system response. This is solved by overlapping the windows, ensuring all data is used in generating the frequency response.

The final consideration taken in measuring the frequency response, is ensuring that the frequency resolution, f_r, of the DFT is sufficiently high to resolve key dynamics of the system. The frequency resolution is given by

$$f_r = \frac{f_s}{N} = \frac{f_s}{f_s T} = \frac{1}{T} \tag{3.1}$$

where f_s is the sampling frequency and N is the number of samples in the DFT, and T is the measurement time for each subrecord. Since the expected nominal eigenmodes of the system can be quite closely spaced, we want a frequency resolution smaller than 0.1 Hz. The measurement time for each subrecord was 18 seconds, giving a frequency resolution of 0.055 Hz.

The methodology for obtaining the frequency response is summarized as follows:

1. Generate a white noise signal using a pseudorandom uniform distribution, and drive one of the patches with this signal for a period of 6 minutes.
2. Measure the time response of the capacative sensors as well as the sensing patches over the 6 minute period.
3. Divide the measurement results into 20 subrecords, where each subrecord is windowed using a Hamming function.
4. Calculate the frequency responses using the DFT's to determine the input to output transfer functions.
5. Repeat for each actuator patch.

3.2.2 Estimating the State Space Parameters of the System

Estimating the state-space parameters of the system is useful in order to extract the mode shapes of the system. These mode shapes can then be used to decouple the system into six SISO systems, for each of which a separate controller can be tuned. Estimation is performed using the MATLAB function `ssest`, which uses prediction error methods to obtain an estimate of the system. To improve the results, and speed of estimation, we can use our knowledge of the system to structure the parameters to be estimated. We know we are dealing with a second-order mechanical system with low damping. Therefore we can express the 6-DOF system in modal coordinates, where the evolution of each mode is given by

$$\ddot{q}_i + 2\zeta_i \omega_i \dot{q}_i + \omega_i^2 q_i = \boldsymbol{B}_i \boldsymbol{u} \tag{3.2}$$

Here q_i represents the i$^{\text{th}}$ modal coordinate, ζ_i is the modal damping factor, and ω_i is the eigenfrequency associated with the mode. $\boldsymbol{B}_i$ represents the i$^{\text{th}}$ row of the input matrix, and $\boldsymbol{u}$ represents the system inputs, being the actuator patch voltages, $[u_1, u_2, u_3, u_4, u_5, u_6]^T$. In state space form we can express the system as

$$\begin{pmatrix} \ddot{\boldsymbol{q}} \\ \dot{\boldsymbol{q}} \end{pmatrix} = \begin{bmatrix} -2\boldsymbol{Z\Omega} & -\boldsymbol{\Omega}^2 \\ \boldsymbol{I}_{6x6} & \boldsymbol{0}_{6x6} \end{bmatrix} \begin{pmatrix} \dot{\boldsymbol{q}} \\ \boldsymbol{q} \end{pmatrix} + \begin{bmatrix} \boldsymbol{B} \\ \boldsymbol{0}_{6x6} \end{bmatrix} \boldsymbol{u} \tag{3.3}$$

$$\begin{pmatrix} \boldsymbol{y} \\ \boldsymbol{w} \end{pmatrix} = \begin{bmatrix} \boldsymbol{0}_{6x6} & \boldsymbol{C} \\ \boldsymbol{0}_{6x6} & \boldsymbol{C_{ee}} \end{bmatrix} \begin{pmatrix} \dot{\boldsymbol{q}} \\ \boldsymbol{q} \end{pmatrix} + \boldsymbol{Du} \tag{3.4}$$

Recall from Figure 1.3 that w is the position of the center of mass of the end-effector, measured using capacative sensors in this case, and y is the output measured using the piezoelectric patches. $\boldsymbol{C}$ is the output matrix, relating the modal coordinates to output, y. $\boldsymbol{C_{ee}}$ relates the modal coordinates to the position of the end-effector, w. From $\boldsymbol{C_{ee}}$, the mode shapes of the end-effector in terms of Cartesian coordinates can be extracted. $\boldsymbol{D}$ is the direct feed-through matrix. The matrices $\boldsymbol{Z\Omega}, \boldsymbol{\Omega}$ are diagonal matrices given by

$$\boldsymbol{\Omega} = \begin{bmatrix} \omega_1 & & 0 \\ & \ddots & \\ 0 & & \omega_6 \end{bmatrix}, \boldsymbol{Z\Omega} = \begin{bmatrix} \zeta_1\omega_1 & & 0 \\ & \ddots & \\ 0 & & \zeta_6\omega_6 \end{bmatrix} \tag{3.5}$$

In MATLAB we can generate a state space model with identifiable coefficients using the function '`idss`'. In this case we require that all parts of the system matrices that are equal to 0, are fixed parameters, as well as the identity matrix in Equation 3.3. In order to run the state-space estimation we also have to provide an initial guess for the non-zero parameters. We can provide a very good guess for the eigenfrequencies as these can be read of from the frequency response results. For the modal damping ratio a value of 1% is assumed, which should be a reasonable estimate for undamped flexure mechanisms. For the input, output and feed-through matrices, B, C, C_{ee}, D, we can use the coefficients extracted from SPACAR as an initial guess. Lastly, important in obtaining a good fit, is to take into account the delay present in the system. The system delay is an input parameter of the function '`idss`'. The delay can be calculated from the phase drop in the obtained frequency response results by using

$$\theta_d = -\omega t_d \tag{3.6}$$

Here the phase change due to delay is given by θ_d, and the time delay in seconds is given by t_d.

3.3 Results

In Figure 3.2 the measured frequency response from the piezoelectric patch actuators 3 and 4 to the end-effector center of mass displacement is plotted, and can be directly compared to the SPACAR results. The responses from actuators 1,2,5 and 6 can be found in appendix A. Due to the symmetry of the system, the response to actuators 1 and 2 is similar to actuator 3, and have therefore been omitted from the main report. The same holds for actuators 5 and 6 in relation to actuator 4. The first thing that can be noticed from Figure 3.2 is that in general there is good agreement between the amplitudes expected from SPACAR and the physical system. For cases where the patch is placed to have good coupling with the displacement direction, the measured amplitude response is at most 50% lower than expected from simulation in the frequency range 5-100 Hz . In the cases where there is bad agreement between the measurements and simulated

results, such as in Fig. 3.2k, this is insignificant because the respective actuator is not designed to couple to the respective output. In this the case the amplitude response is still a factor 100 lower than the transfer from actuator 3 to the z position. Note that the SPACAR-response is not visible in the plot due to it being below the y-limits.

The next takeaway from the results in Figure 3.2 is that the observed locations of the resonance peaks of the nominal modes are higher than expected from the SPACAR and FEA simulations. For example in Fig. 3.2e the SPACAR resonance lies at 14.2 Hz while the measured resonance occurs at 15.2 Hz. At low frequency the transfer function approximates the inverse of the stiffness, $\frac{1}{k}$. It can be seen that the low frequency amplitude response is lower than expected with SPACAR, indicating a higher stiffness of the system in that direction. This explains why the resonance frequencies are higher than expected. Potential sources of this extra stiffness could be pretension in the system due to misalignment in the assembly phase, or parasitic stiffness present due to the cables connecting to the capacitive sensors and piezoelectric patches.

There are more resonances present in the actuator to end-effector response, which is best highlighted in Figure 3.2b. Between 1 and 2 Hz we see a first resonance caused by the optical table upon which the entire set-up is positioned. At approximately 12 Hz we see a peak, which consists of 2 closely spaced eigenfrequencies. These are 2 nominal mode shapes corresponding to translations in the x-y plane. The next resonance seen is the θ_z mode coupling into the x-displacement. This is not surprising, as patch 4 also couples into the θ_z mode. Next, two closely spaced peaks are seen at 20 and 21 Hz. These are the nominal modes in relation to θ_x and θ_y, coupling into x-displacement. The extra coupling of other nominal modes should not pose a large problem when the system is decoupled. At 60 Hz a first high frequency parasitic frequency is present. Upon further investigation further high frequency resonances are found at 70, 88, 110, 141 and 196 Hz. In this work, the short-stroke stage is clamped in its end-stops, so that measuring plate of the short-stroke is stationary in reference to the metrology frame. The parasitic modes are most likely due to the limited stiffness of the clamping, leading to vibration of the reference measurement plate. This also explains why 6 parasitic modes are observed, one mode for each translation and rotation of the measurement plate. While the resonance should not be a problem for the controller implemented in this work, it will pose a problem for the bandwidth of the controller of the short-stroke mechanism. If the parasitic resonances are indeed due to the limited clamping stiffness of the short-stroke, these resonances will disappear once the short-stroke is free to move, and are then not a problem. In short, in the measured results more resonances are seen then expected from SPACAR. In the cases where other nominal modes are coupling into the movement, this should not be problematic. The parasitic frequencies are most likely not problematic, but this will only be evident in future work, when the short-stroke is operated simultaneously with the PPF controller.

The actuator 1 to sensor 1 frequency response is plotted in Figure 3.3. This represents a typical collocated response, with lack of high-frequency roll-off, and closely spaced resonances and anti-resonances. Although the behavior is as expected the amplitude response is a factor 10 lower than the SPACAR simulation. This can be explained by the fact the piezoelectric patches are integrated close to the clamping point of the flexures. In SPACAR the anticlastic bending of the flexures is not constrained, which leads to extra expected coupling which is not seen in reality. In the phase response we see the effects of the high-pass filter, with a corner frequency of just below 1 Hz, located in the charge amplifier. This explains the additional phase lead at 1-6 Hz. The high frequency phase drop is the effect of delay on the system. Using Equation 3.6 the delay is calculated to be approximately 0.6 ms. This value is similar for all sensor to actuator responses.

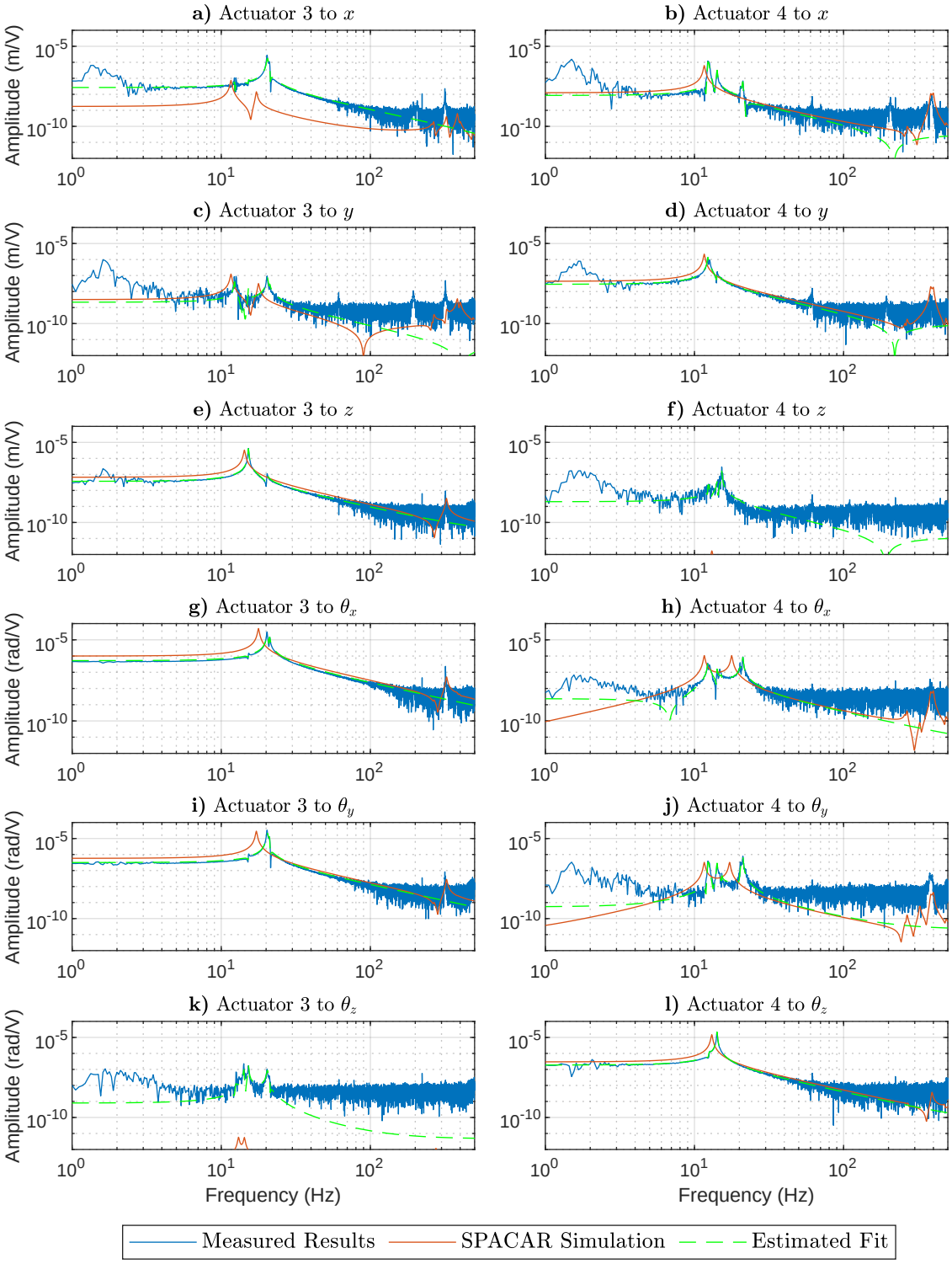

Figure 3.2: Results of the actuator to end-effector system identification.

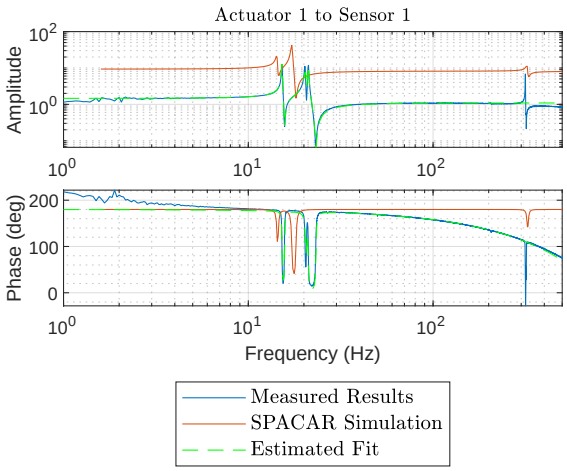

Figure 3.3: Actuator 1 to sensor 1 frequency response. This illustrates a typical collocated response, with lack of high-frequency roll-off.

In general, the estimated fit matches well with the measured data. It can be seen that the fit parameters correctly follows the location and approximate height of the nominal resonances. The fit also characterizes the coupling of nominal modes, as seen in Figure 3.2b. The cross transfers, such as Figure 3.2j, are also fit well. The estimated fit ignores the high frequency noise, and fits well to the dynamics of the mode shapes. It can be concluded that the fit of the second order model accurately describes the measured system response in the frequency range 6-100 Hz. In Figure 3.3 it can also be seen, in the phase response, that the input delay of 0.6 ms specified for the fit, also accurately matches the system behavior.

The identified system parameters such as the mode shapes, frequencies and damping ratio are listed in Table 3.1. These results agree with the observed frequency response. For instance modes 1,2,3,5 and 6 all have some degree of coupling to the x-direction. This is exactly why we saw the presence of all these resonances in Figure 3.2b. The estimated modal damping ratios show that the assumption of 1% modal damping in the SPACAR simulations was realistic. Modes 5 and 6 of the system lie above 20 Hz, which is outside of the design specifications. While not an immediate problem for the purpose of this work, it can be problematic for the performance of the short-stroke stage. This can readily be resolved by adding mass to the end-effector, as far away from the rotation axis as probable. There are two locations this can be done. First of all mass can be added to the bolts which function as end-stops. Second, on top of the end effector three points with bolt holes are already present, where additional mass can be bolted to the end-effector. It should thus be possible to bring the frequencies to within specification.

From this section a couple of important conclusions can be drawn. While the resonant frequencies of the built assembly are higher than the modelled design, the system behavior is similar to the dynamic model from SPACAR. Especially the amplitude response from actuator to end-effector position is predicted well by SPACAR. Additionally, state-space estimation using structured parameters can give good estimates of the state-space matrices, modes, and mode-shapes. This is useful for controller design. Some extra time is needed to investigate and fix the low parasitic frequency around 60 Hz, and given more time the out of specification nominal modes can also be brought into specification.

Mode number	Frequency (Hz)	ζ	Mode Shape
1	12.3	0.52%	$-396\hat{\boldsymbol{x}} - 478\hat{\boldsymbol{y}}$
2	12.5	1.1%	$553\hat{\boldsymbol{x}} - 609\hat{\boldsymbol{y}}$
3	14.2	0.46%	$32\hat{\boldsymbol{x}} - 35\hat{\boldsymbol{y}} - 93\hat{\boldsymbol{\theta}}_{\boldsymbol{z}}$
4	15.2	0.44%	$-447\hat{\boldsymbol{z}}$
5	20.4	1.0%	$-9\hat{\boldsymbol{x}} - 8\hat{\boldsymbol{y}} - 27\hat{\boldsymbol{\theta}}_{\boldsymbol{x}} + 31\hat{\boldsymbol{\theta}}_{\boldsymbol{y}}$
6	21.0	0.50%	$12\hat{\boldsymbol{x}} - 11\hat{\boldsymbol{y}} - 38\hat{\boldsymbol{\theta}}_{\boldsymbol{x}} - 37\hat{\boldsymbol{\theta}}_{\boldsymbol{y}}$

Table 3.1: The identified nominal eigenfrequencies, modal damping ratio ζ, and the mode shape.

4 Control Design

4.1 Introduction

In this chapter the implementation of the controller, to achieve the desired vibration suppression, is discussed. Looking back at Figure 1.3, reminds us of the control problem. We have a system plant, P, for which we wish to attenuate the transfer from unknown disturbance, d, to the end-effector position, w. Specifically, we want to suppress the vibrations at the nominal eigenfrequencies of the system. To achieve this, we make use of collocated piezoelectric patches, forming a piezoelectric bimorph. Since we have a 6-DoF system with 6 actuators and 6 sensors this is a MIMO control problem. To simplify the problem, decoupling can be used to go from 1 MIMO system to 6 SISO systems, for each of which a controller has to be designed. The most natural choice for the decoupling method is to use modal decoupling, as by definition, each nominal eigenfrequency has a linearly independent modeshape. Meaning that a modally decoupled system allows us to act on each eigenfrequency individually. The method of finding the input and output decoupling matrices T_u and T_y is detailed in the first part of this chapter.

The second part of this chapter focuses on the controller used for achieving the resonance suppression. Multiple control strategies are possible. One common method to add damping to a structure is to implement some form of negative velocity feedback. In 2005, Holterman et al. utilised integral force-feedback to suppress multi-DoF vibrations in a lens-suspension stage [8]. Similarly in their work they made use of collocated actuator-sensor pairs, and with the passive control law were able to guarantee robust control, even in the case of imperfect decoupling. However, because the controller is a simple integrator multiplied with a control gain, the control effort is not allocated optimally to the specific frequency range of interest. This is a key strength of positive position feedback (PPF). The controller has the form of a second order low-pass filter. This provides a high control gain and thus damping at the resonance of the controller, while keeping the control gain low at lower, less relevant frequencies. It also provides better high-frequency roll-off, important because collocated piezoelectrics typically do not have this behavior in the system transfer function for parasitic frequencies. PPF is a well-established resonant control technique introduced by Goh in 1983 [6]. More recently it has been utilised by Seinhorst et al. to show the potential of using active materials in damping of undesired parasitics [16]. In his work, Seinhorst also derives the H_2 optimal controller parameters in a generalised form [15]. Based on this work the controller is designed and tuned in the second part of this chapter.

4.2 Decoupling

By fitting a second order system in modal form in chapter 3, the decoupling into 6 SISO systems is not a very complex process. The MIMO system is given by

$$\ddot{q} + 2\boldsymbol{Z\Omega}\dot{q} + \boldsymbol{\Omega}^2 q = Bu \tag{4.1}$$

If we introduce a set of virtual actuators given by $v_a = Bu$ then Equation 4.1 becomes

$$\ddot{q} + 2\boldsymbol{Z}\boldsymbol{\Omega}\dot{q} + \boldsymbol{\Omega}^2 q = v_a \tag{4.2}$$

Since $\boldsymbol{Z}, \boldsymbol{\Omega}$ are diagonal matrices, we have 6 independent equations defining the evolution of the MIMO system. Each virtual actuator actuates only one mode of the system.

The relation between the modal coordinates, q, and the sensor outputs, y, is given by

$$y = Cq + Du \tag{4.3}$$

We can construct a virtual sensor given by $v_s = C^{-1}(y - Du) = q$ to measure the current state of the system. Since each virtual sensor only measures one modal coordinate, and each virtual actuator acts on only one unique modal coordinate, the transfer $P_{\text{dec}} = \frac{v_s}{v_a}$ is a decoupled, diaganolized system. Let the original plant be designated by P, we have

$$y = Pu \tag{4.4}$$

$$v_s = C^{-1}(Pu - Du) \tag{4.5}$$

$$v_s = C^{-1}(P - D)B^{-1}v_a \tag{4.6}$$

$$P_{\text{dec}} = C^{-1}(P - D)B^{-1} \tag{4.7}$$

In this form we can recognize $T_y = C^{-1}$ and $T_u = B^{-1}$ as our decoupling matrices. This requires B and C to be invertible matrices. B and C are square matrices, where the amount of sensors and actuators is equal to the number of modes to be suppressed. Due to the system design, all modes can be measured or actuated linear independently, B and C will therefore be full rank. Since, B and C are square and full rank, they can be inverted. In many cases the direct feed-through matrix, D, is negligible. This is, however, not the case in the case of collocated actuator-sensor pairs, and from a mathematics perspective can not just be ignored. Nevertheless, in the implementation it was found that when taking into account the direct feed-through term, the system had worse high frequency attenuation. Therefore, the decoupled system used in this case is

$$P_{\text{dec}} = C^{-1}PB^{-1} \tag{4.8}$$

The bode plot for the virtual actuator to virtual sensor transfers is shown in Figure 4.1. Each virtual sensor measures one of the nominal mode shapes. This can be seen from the fact that the resonance in one given row, is always at the same frequency (ignoring the low frequency optical table modes, and the higher frequency parasitic modes). The elements on the diagonals are dominant within each row. The amplitude response at the eigenfrequency is a factor 10 greater for the diagonal elements. Figure 4.2 shows the transfer function from the virtual actuators to the measured modal displacement of the end-effector. This is measured using the capacitive sensors. Here, we can see similar decoupling performance. Near 1-2 Hz the decoupling is poor as the optical table mode is dominant here. But from 10 - 20 Hz we see dominance of the transfers on the diagonals, with a factor of around 10 at the resonance.

The quality of the decoupling can be quantified using the relative gain array (RGA), and by calculating the RGA number. The RGA, Λ is given by [5]

$$\Lambda = P_{\text{dec}} \circ P_{\text{dec}}^{-T} \tag{4.9}$$

where $\circ$ represents the Hadamard product, and P_{dec}^{-T} is the inverse transpose of P_{dec}. The RGA number, n, can then be calculated using

$$n = \sum_i \sum_j |I - \Lambda|_{ij} \tag{4.10}$$

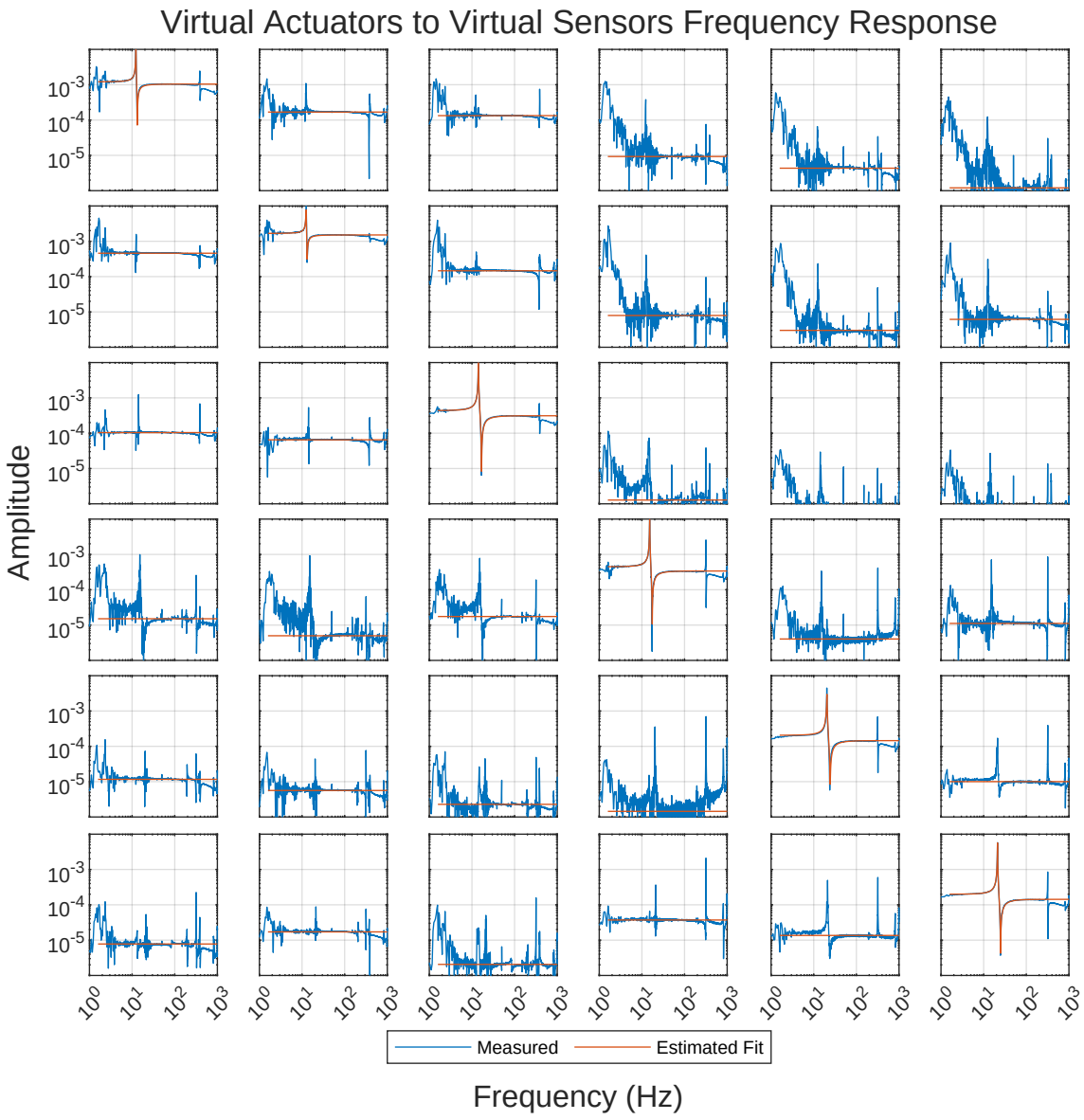

Figure 4.1: Frequency response of the actuator to sensor transfer for the decoupled plant, P_{dec}.

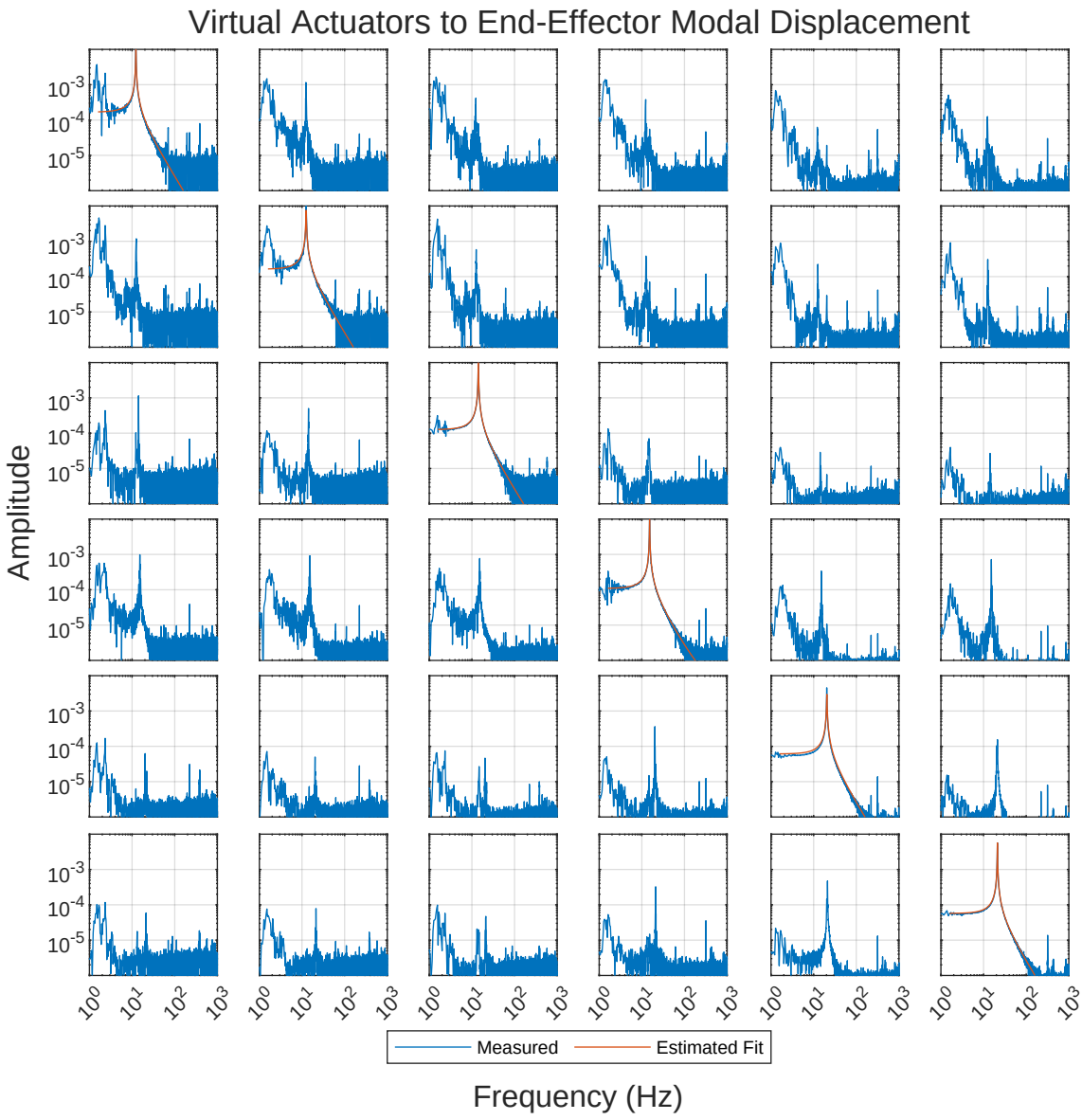

Figure 4.2: Frequency response of the actuator to end-effector transfer for the decoupled plant, P_{dec}.

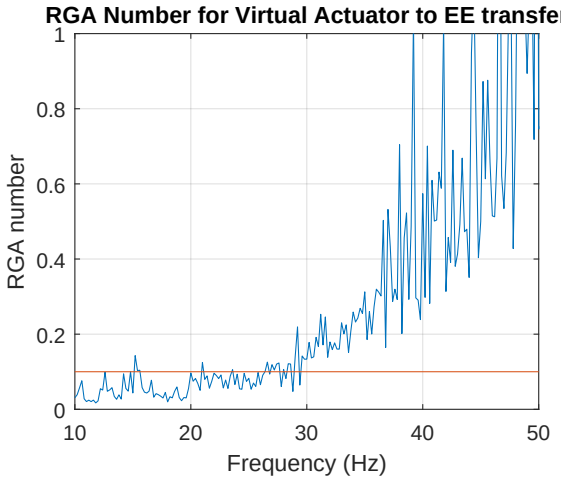

Figure 4.3: RGA number of the system at different frequencies.

A rule of thumb for a decoupled system is to have $n < 0.1$. The RGA for the transfers from virtual actuators to modal displacement of the end-effector is plotted in Figure 4.3. As can be seen, in the frequency range 10-25 Hz the system can be considered decoupled. After this the RGA number starts to increase, signifying that the decoupling becomes worse as frequency increases. This can be expected, as we decouple at the first 6 eigenfrequencies of the system. In their frequency regime these eigenmodes will dominate the system response. This is no longer true at high frequencies as at this point higher parasitic frequencies, with different eigenmodes, will start to dominate the system response. This degradation of the decoupling should, however, not pose a problem for controller design, as we expect our controller needs to work in the same frequency regime, in which the modal decoupling is performed. This is an advantage of using PPF, which is active in a small band around the resonance. The roll-off at high frequencies ensures that the controller does not work at frequencies where the decoupling is no longer valid.

To summarize, in this section we performed modal decoupling by defining virtual actuators and virtual sensors on which the controller will act. The decoupling is not perfect, but should be good enough in order to allow us to treat the system as the combination of 6 SISO systems with one eigenmode. We can now individually design and tune a controller to suppress the vibrations at the eigenfrequency of each SISO system.

4.3 Positive Position Feedback

A positive position feedback controller is given by [15]:

$$C(s) = \frac{k_c \omega_c^2}{s^2 + 2\zeta_c \omega_c s + \omega_c^2} \tag{4.11}$$

Where k_c is the controller gain, ζ_c the controller damping ratio and ω_c is the eigenfrequency of the controller. At the resonance the controller provides 90 degrees of phase lag. In combination with the positive feedback loop this provides a 90 degree phase lead, which adds the damping to the system [15]. Tuning the controller is done by picking the parameters ζ_c, ω_c, and k_c. Typically, w_c is chosen to be at or near the resonance which should be suppressed. Seinhorst derived a H_2 optimal controller for a second-order system with direct-feedthrough from actuator to sensor [15]. Our system is of the same form, and therefore the results from his work can be used to calculate the optimal parameters for our controller.

The optimal controller parameters are determined by picking g and the system parameters γ_{yu}, γ_{yd} and γ_{wu}. g is decided by specifying a desired gain margin, given by $1 - g$. In this case, we chose $g = 0.6$. The system parameters are obtained from the low and high frequencies asymptotes of the plant P_{ij}:

$$\gamma_{ij} = \frac{P_{ij}(\omega = \infty)}{P_{ij}(\omega = 0) - P_{ij}(\omega = \infty)} \tag{4.12}$$

Note that in this case P refers to one of the diagonal elements of the decoupled plant P_{dec}. In this case the system parameters are calculated from the estimated fit in chapter 3. For the transfer from disturbance to sensor no measurements were completed, therefore the system parameter γ_{yd} was determined from the SPACAR simulation. The controller parameters can then be determined from the system parameters as follows:

$$k_c = \frac{g}{1 + \gamma_{yu}} \frac{\gamma_{yu}}{P_{yd}(\omega = \infty)} \tag{4.13}$$

$$\omega_c = \frac{\omega_n}{\sqrt{1 - g\frac{\gamma_{yu} - \gamma_{yd} - \gamma_{wu}}{1 + \gamma_{yu}}}} \tag{4.14}$$

$$\zeta_c = \frac{1}{2}\sqrt{\frac{g}{1-g}} \frac{1 - g(\frac{\gamma_{yu} - \gamma_{yd} - \gamma_{wu} - \gamma_{yd}\gamma_{wu}}{1 + \gamma_{yu}})}{\sqrt{1 + \gamma_{yu}}\sqrt{1 - g\frac{\gamma_{yu} - \gamma_{yd} - \gamma_{wu}}{1 + \gamma_{yu}}}} \tag{4.15}$$

Where ω_n is the eigenfrequency of the mode to be damped. Applying this methodology to our plant gives the following parameter set for the 6 decouples SISO systems.

$$\begin{aligned}
[\zeta_{c,1}, \ldots, \zeta_{c,6}] &= [0.16, 0.13, 0.26, 0.23, 0.26, 0.25] \\
[\frac{\omega_{c,1}}{\omega_{n,1}}, \ldots, \frac{\omega_{c,6}}{\omega_{n,6}}] &= [1.41, 1.46, 1.28, 1.32, 1.28, 1.29] \\
[k_{c,1}, \ldots, k_{c,6}] &= [497, 359, 1370, 1340, 2916, 3005]
\end{aligned}$$

The approximate values of the controller parameters agree with the results from Seinhorst. In that case the optimal values for $g = 0.6$ were $\frac{\omega_c}{\omega_n} = 1.6$ and $\zeta_c = 0.19$. The systems are clearly different, so the exact same values should not be expected, but it is indicative that the obtained controller values are reasonable.

For the first decoupled eigenmode the controller C, the plant P, and the open loop PC have been plotted in Figure 4.4. This illustrates the introduced roll-off by the controller in the high-frequency region. Bode stability is guaranteed by the fact that the phase of the open-loop remains bounded within $\pm 180°$, at the point where the open loop gain is greater than 1.

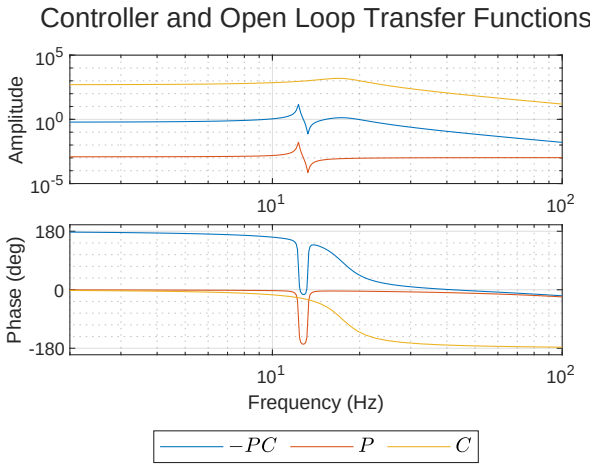

Figure 4.4: The open loop of the implemented controller for virtual actuator 1 to virtual sensor 1.

5 Results

In Figure 5.1a the normalised impulse response for the system is plotted for the case that the controller is turned on, and off. For these measurements, a disturbance was applied to the optical table by hand. To make the responses comparable the peak of the resulting impulse response was normalised to 1. The system performance is measured using the capacitive sensors, where the results are transformed from cartesian directions to the modal directions, $\boldsymbol{\phi}$, using

$$\left(\phi_1, \phi_2, \phi_3, \phi_4, \phi_5, \phi_6\right)^T = \boldsymbol{C}_{\boldsymbol{ee}}^{-1} \left(x, y, z, \theta_x, \theta_y, \theta_z\right)^T \tag{5.1}$$

In Figure 5.1a it can be seen that the controller is damping the system response. When the controller is turned off, the absence of any meaningful damping is clear. After 5 seconds there is still a large vibrating component measurable at the frequency of mode 1 (12.3 Hz). When the controller is turned on, any noticeable effect of the resonance has been damped out after 1 second. The remaining vibration visible is a low frequency 1 - 2 Hz vibration corresponding to the eigenfrequency of the optical table. This is to be expected as any disturbing force on the optical table will also excite that optical table mode. Figure 5.1b shows the voltages applied across the actuation patches in order to apply the vibration supppression, not only of mode 1, but of all 6 vibration modes. The applied voltages remain within ± 20V. The operating range for the patches is -50 to 200 Volts. As such, we wish to remain within the range -50 to 50V, meaning that there is still more than double the control budget left.

The power spectral density (PSD) of the response of every mode is plotted in Figures 5.2a-f. To obtain these measurements, a white-noise force-disturbance was applied by the actuators of the short stroke mechanism to the optical table. The forces present in the white-noise signal were limited to 25% of the maximum for every short stroke actuator. For every mode shape we can see substantial attenuation of the nominal resonance. The resonance gets reduced to similar levels of the neighboring frequencies. Some small spill-over effects can be seen for modeshapes 1 and 2, directly after the resonance. Noteworthy is the lack of roll-off after the first nominal mode of the suspension mechanism. This can be explained by the fact that the disturbance is not only applied to the suspension mechanism, but also to the measuring plate of the short-stroke, which is clamped in place. The clamped connection is much stiffer than the suspension mechanism, and therefore vibrations will only be attenuated after the resonance of the measuring plate. This can be seen in Figure 5.2b, where vibrations are attenuated after

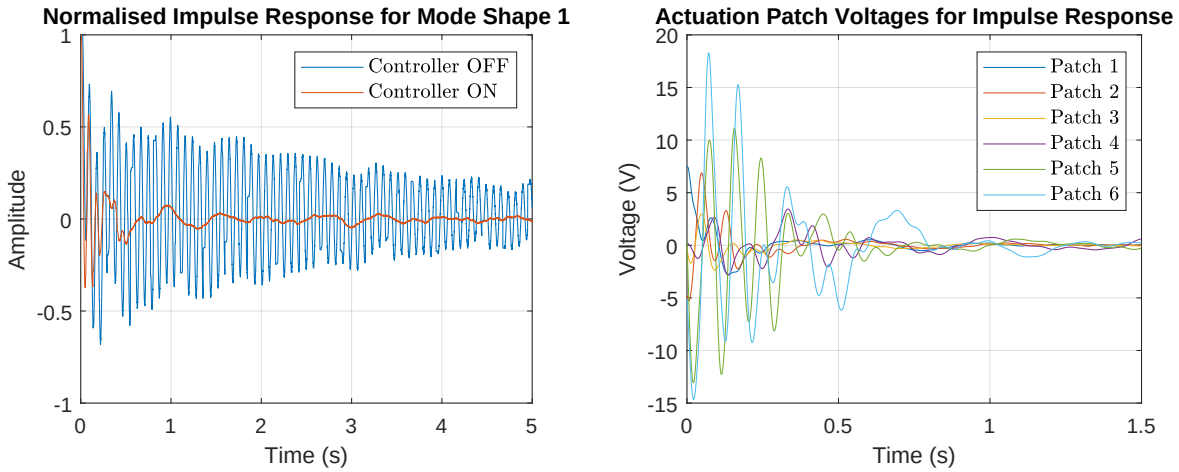

(a) Comparison of the normalised impulse response with and without controller.

(b) Actuation voltages applied to piezoelectric patches to achieve controlled response.

Figure 5.1: Impulse response of controlled and uncontrolled system, with actuation voltages required to achieve controlled response.

the first parasitic frequency at 60 Hz. The existence of 6 parasitic resonances matches the 6 constraints needed to clamp the measuring plate. This supports the claim that the parasitic resonances are indeed due to the limited stiffness of clamping of the measuring plate, and will thus likely not be a problem for the bandwidth of the short-stroke controller.

In Figures 5.3a and b another PSD is plotted, this time the disturbance is an impulse force disturbance on the optical table. From these plots it is possible to estimate the Q-factor by measuring the bandwidth of the peak at half power. The Q factor is then given by

$$Q = \frac{f_r}{\Delta f} \tag{5.2}$$

Where f_r is the resonance frequency and Δf the peak width at half power. From the Q factor the damping ratio can be calculated as $\zeta = \frac{1}{2Q}$. The estimated damping ratios are $\zeta_1 = 0.11$, $\zeta_2 = 0.09$ and $\zeta_5 = 0.13$ For the other mode shapes it is not possible to estimate a damping ratio using this method.

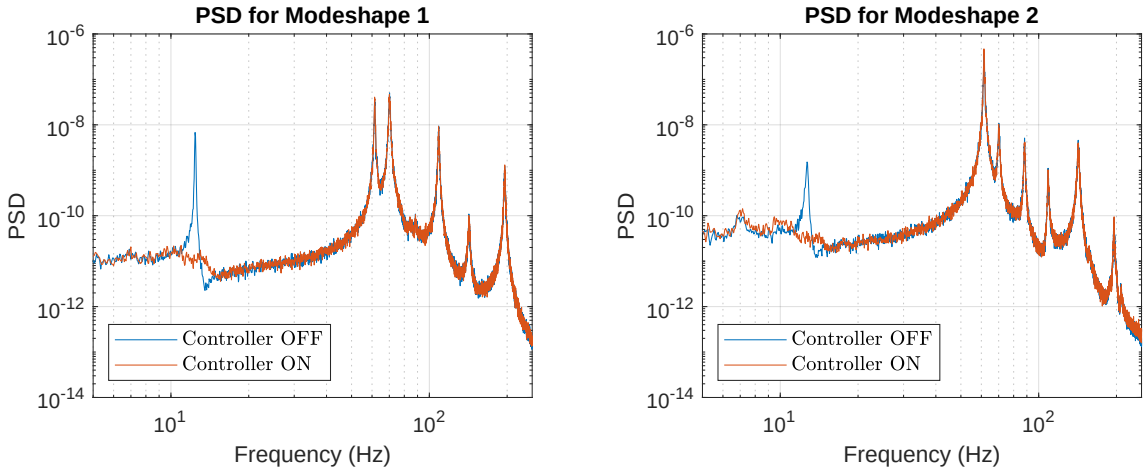

(a)

(b)

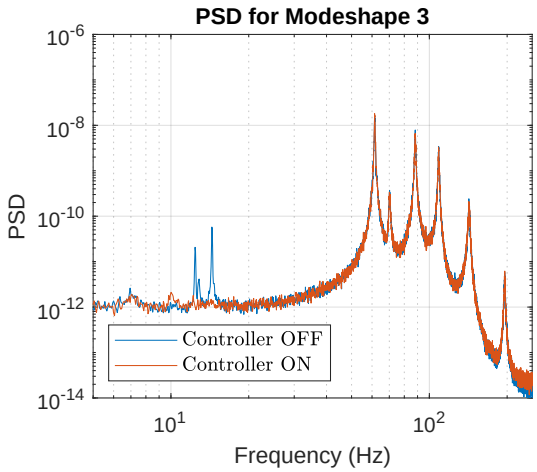

(c)

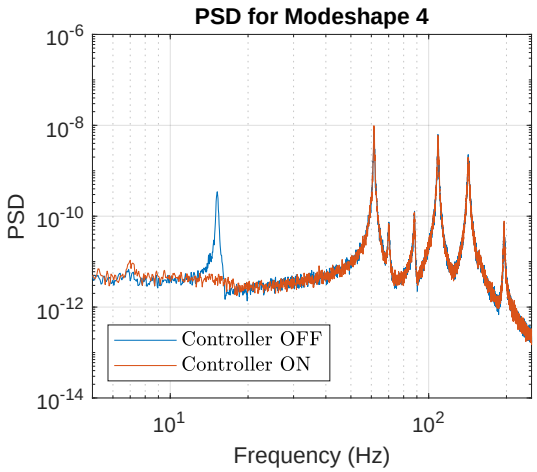

(d)

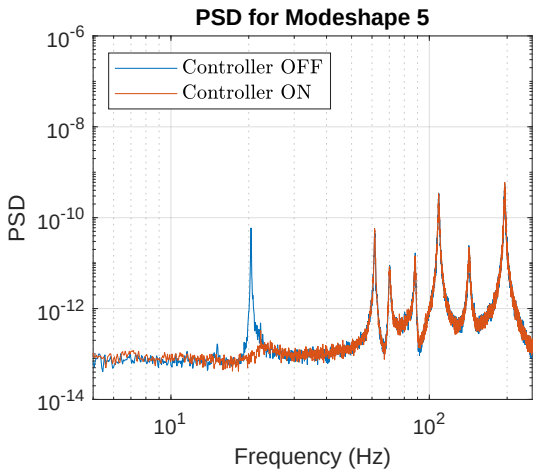

(e)

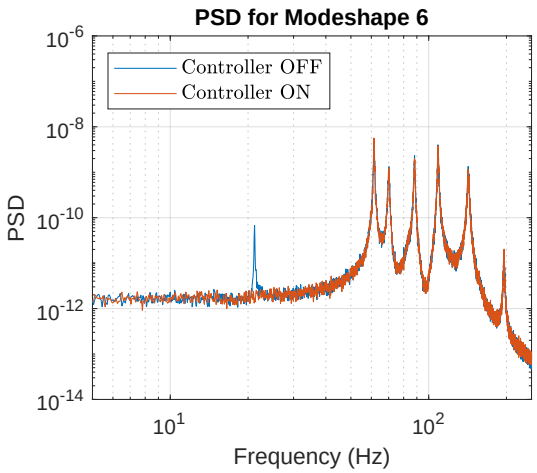

(f)

Figure 5.2: Power spectral density of each measured mode shape with the input disturbance being a white-noise force disturbance applied by the actuators of the short-stroke stage.

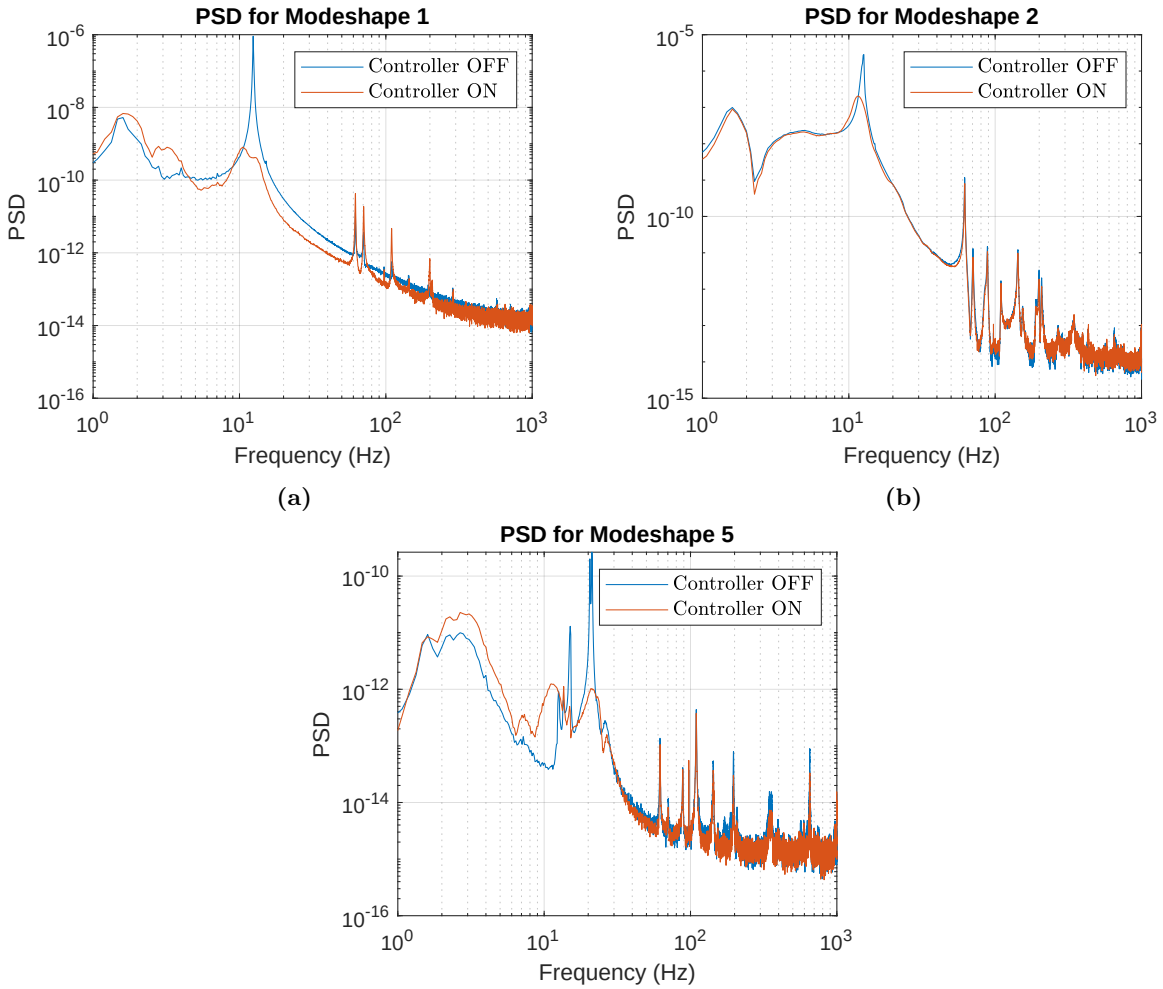

Figure 5.3: Power spectral density of mode shapes 1,2 and 5, calculated from an impulse response. From these figures damping ratios can be calculated.

6 Conclusion

The aim of this work was to test the viability of applying piezodamping on a 6-DoF isolation frame. The first part of this work focused on designing the suspension with integrated piezoelectric patches. Key to success of the design phase was the utilization of the SPABS extension to the multibody software SPACAR. The coupling between patches and the end-effector position could be determined from this, and thereby ensure measurable signals, and attainable attenuation. In the second part, system identification and structured parameter estimation were used to determine the resonances and associated mode shapes. Using modal decoupling the MIMO system was decoupled into 6 SISO systems. For each SISO system a PPF controller was tuned using the H2 optimal controller parameters.

The results indicate that the project was a success, with some points requiring improvement. For the design, the found resonances of the compliant modes were higher than expected, whereby two are slightly outside the design specifications. In the transfer function 6 parasitic frequencies were found in the range 60 Hz to 197 Hz, which is below the required specification of 200 Hz. All other design specifications were met. Despite these issues, a functioning controller was designed and implemented. In each nominal direction the resonance was substantially suppressed. The achieved damping ratio is between 9% and 13%. This is equivalent to the performance of an optimally tuned TMD with a mass ratio of 10% [3]. The absence of this additional mass, the tunability, and easy integration of the piezoelectric patches within flexure mechanisms can make this a more suitable solution in many cases. Especially if long term performance is required in a space limited application.

Perhaps more importantly, this work demonstrates that with the current tools available a successful end-result is achievable within a reasonable time frame. As shown in chapter 3 the coupling predicted from the generated dynamical models in SPACAR is in accordance with the measurements from the system identification. In fact, for this work some system properties for tuning the PPF controller were estimated from SPACAR. The functioning of the controller demonstrates that the estimated system properties from SPACAR were reasonably accurate. This is important, because the computational efficiency of SPACAR allows for design space exploration and rapid iteration to create a viable design. At the end of the design phase a conventional FEA can then be used for validation purposes. Another important point, the method is somewhat robust to modelling errors. The realized resonance frequencies of the suspension being higher than expected formed no problem for the implementation of the piezoelectric damping, due to the identification process. From this work a method can be distilled, which when followed should lead to a successful end-result. This makes it more likely for this technique to be adoptable in industry.

Although the general result is a success, there is still much work that can be done to improve the result. Improved measurements of the disturbance to end-effector transfer can be used to evaluate the tuning of the controller, and potentially improve the results. To accurately validate the result of this work, it is meaningful to get the full system in operation, with the short stroke in operation at the same time as the piezoelectric patches. In this form the effects on the average positioning error of the short-stroke relative to the metrology frame can be measured directly.

7 Recommendations

In this section some recommendations for further development of the solution, and further research are listed.

- First of all, the short stroke controller needs to be re-tuned, and the software adapted to be able to run the short stroke and piezoelectric damping simultaneously. When this is done, it can be checked if the parasitic resonances between 60 and 197 Hz have indeed been resolved.
- The impact of the piezoelectric damping should be measured more accurately, with the short-stroke in operation. This will result in quantitative results in the position tracking performance, which can further support the industrial relevance of this technique.
- A source of performance improvement could be reducing the resonance frequency of the outside-of-specification eigenfrequencies. While not a problem for the PPF control performance, it does have an effect on the short stroke performance as lower frequencies are easier to follow. One way this can readily be done is by adding mass to the metrology frame.
- Performance improvement could also be achieved by using disturbance feed-forward control. The accelerations of the optical table should then be measured and then compensated by the patches [7].
- Another interesting option would be to research the potential of cancelling the reaction forces from the short stroke stage using the patches from the metrology frame, as described by Spanjer et al [18].
- Improvements are also possible to the completed mechanical design. A gravity compensator could be considered to reduce stresses on the flexures. Moreover, it would be interesting to implement the design of concept 2, as shown in Figure 2.2b. This would eliminate the need for an intermediate body, saving a lot of material, mass and space. This effect snowballs, as it also means the outside frame can be designed smaller and more compact.

References

[1] Braun, S. (2001). Windows. In Braun, S., editor, *Encyclopedia of Vibration*, pages 1587–1595. Elsevier, Oxford.

[2] Brouwer, D. M., de Jong, B. R., and Soemers, H. M. (2010). Design and modeling of a six dofs mems-based precision manipulator. *Precision Engineering*, 34:307–319.

[3] Connor, J. (2003). *Introduction to Structural Motion Control*, chapter Tuned Mass Damper Systems. Prentice Hall Pearson Education.

[4] Dunning, A. G., Tolou, N., and Herder, J. L. (2011). Review article: Inventory of platforms towards the design of a statically balanced six degrees of freedom compliant precision stage. *Mechanical Sciences*, 2:157–168.

[5] Engell, S., Trierweiler, J. O., Völker, M., and Pegel, S. (2004). *Chapter C4 - Tools indices for dynamic I/O-controllability assessment control structure selection*, volume 17, pages 430–463. Elsevier.

[6] Goh, C. J. (1983). Analysis and control of quasi distributed parameter systems.

[7] Hakvoort, W. B. and Beijen, M. A. (2023). Filtered-error rls for self-tuning disturbance feedforward control with application to a multi-axis vibration isolator. *Mechatronics*, 89:102934.

[8] Holterman, J. and de Vries, T. J. (2005). Active damping based on decoupled collocated control. *IEEE/ASME Transactions on Mechatronics*, 10:135–145.

[9] Holterman, J. and Groen, P. (2013). *An Introduction to Piezoelectric Materials and Applications*. Stichting Applied Piezo.

[10] Hopkins, J. B. and Culpepper, M. L. (2011). Synthesis of precision serial flexure systems using freedom and constraint topologies (fact). *Precision Engineering*, 35.

[11] Jonker, J. B. and Meijaard, J. P. (1990). *SPACAR — Computer Program for Dynamic Analysis of Flexible Spatial Mechanisms and Manipulators*, pages 123–143. Springer Berlin Heidelberg.

[12] JPE (2023). 3 parallel folded leaf springs. [Online; accessed 2024].

[13] Lemmen, B., Smeenk, R., and Janno, L. (2023). Vibration isolation for nanometer measurement device. *Mikroniek*.

[14] Seinhorst, B., Nijenhuis, M., and Hakvoort, W. (2024a). A beam element with arbitrary active cross-sections for multibody simulation of large deflection flexure mechanisms. *To be published*.

[15] Seinhorst, B., Nijenhuis, M., and Hakvoort, W. (2024b). Gain margin constrained h2 and h∞ optimal positive position feedback control for piezoelectric vibration suppression. *To be published*.

[16] Seinhorst, B., Nijenhuis, M., and Hakvoort, W. B. J. (2022). Feasibility of active material vibration suppression in a large stroke flexure hinge. *IFAC-PapersOnLine*, 55:166–171. 9th IFAC Symposium on Mechatronic Systems MECHATRONICS 2022.

[17] Soemers, H. (2010). *Design Principles for Precision Mechanisms*. UniversityOfTwente.

[18] Spanjer, S., Kelder, R., and Hakvoort, W. (2023). Active vibration isolation with integrated virtual balance mass for a motion stage.

[19] Wang, C., Xie, X., Chen, Y., and Zhang, Z. (2016). Investigation on active vibration isolation of a stewart platform with piezoelectric actuators. *Journal of Sound and Vibration*, 383:1–19.

[20] Yang, Z., Lee, R., and Hopkins, J. B. (2022). Hexblade positioner: A fast large-range six-axis motion stage. *Precision Engineering*, 76:199–207.

A System Identification for Actuators 1, 2, 5 and 6

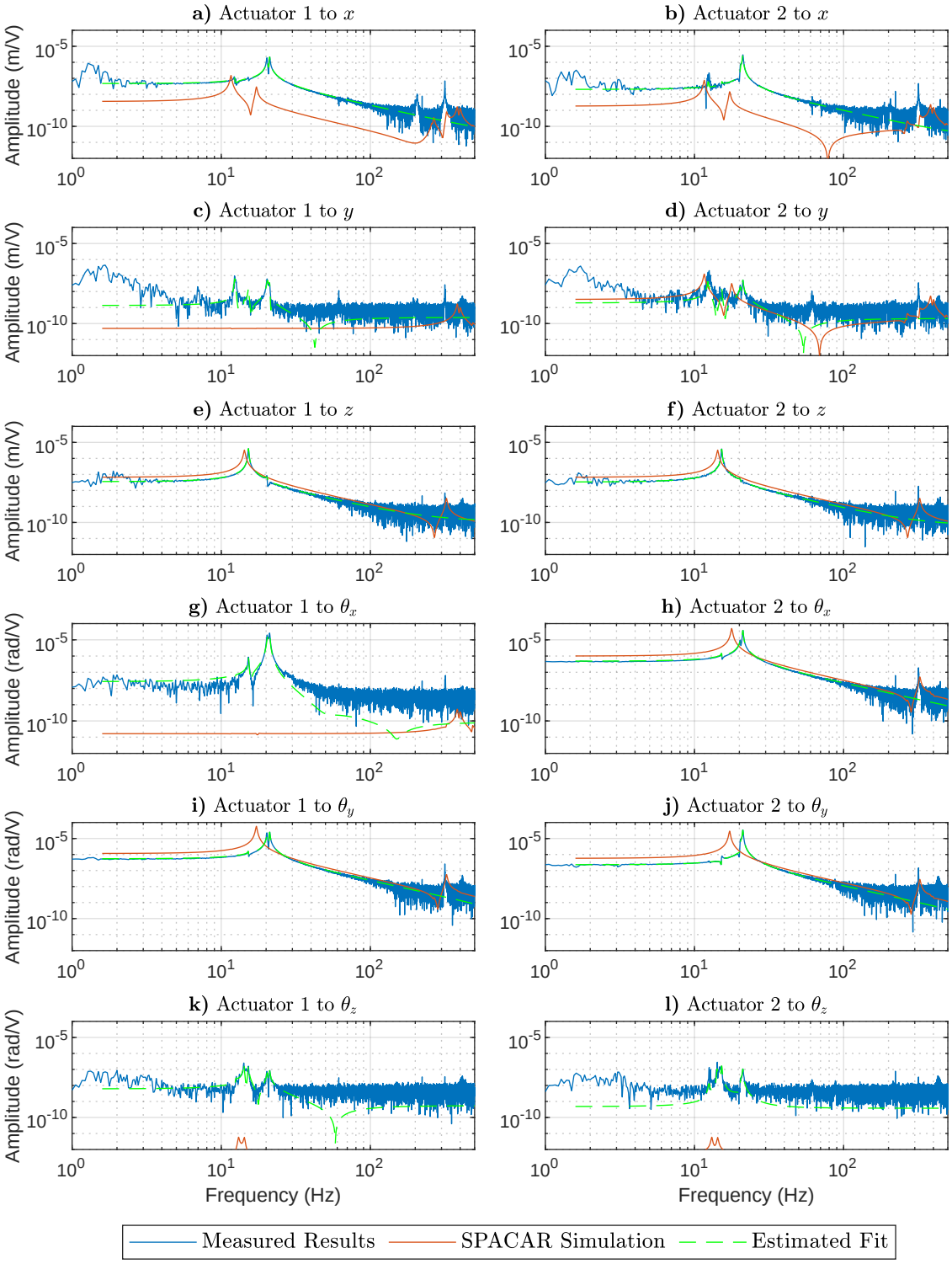

Figure A.1: System Response for Actuators 1 and 2

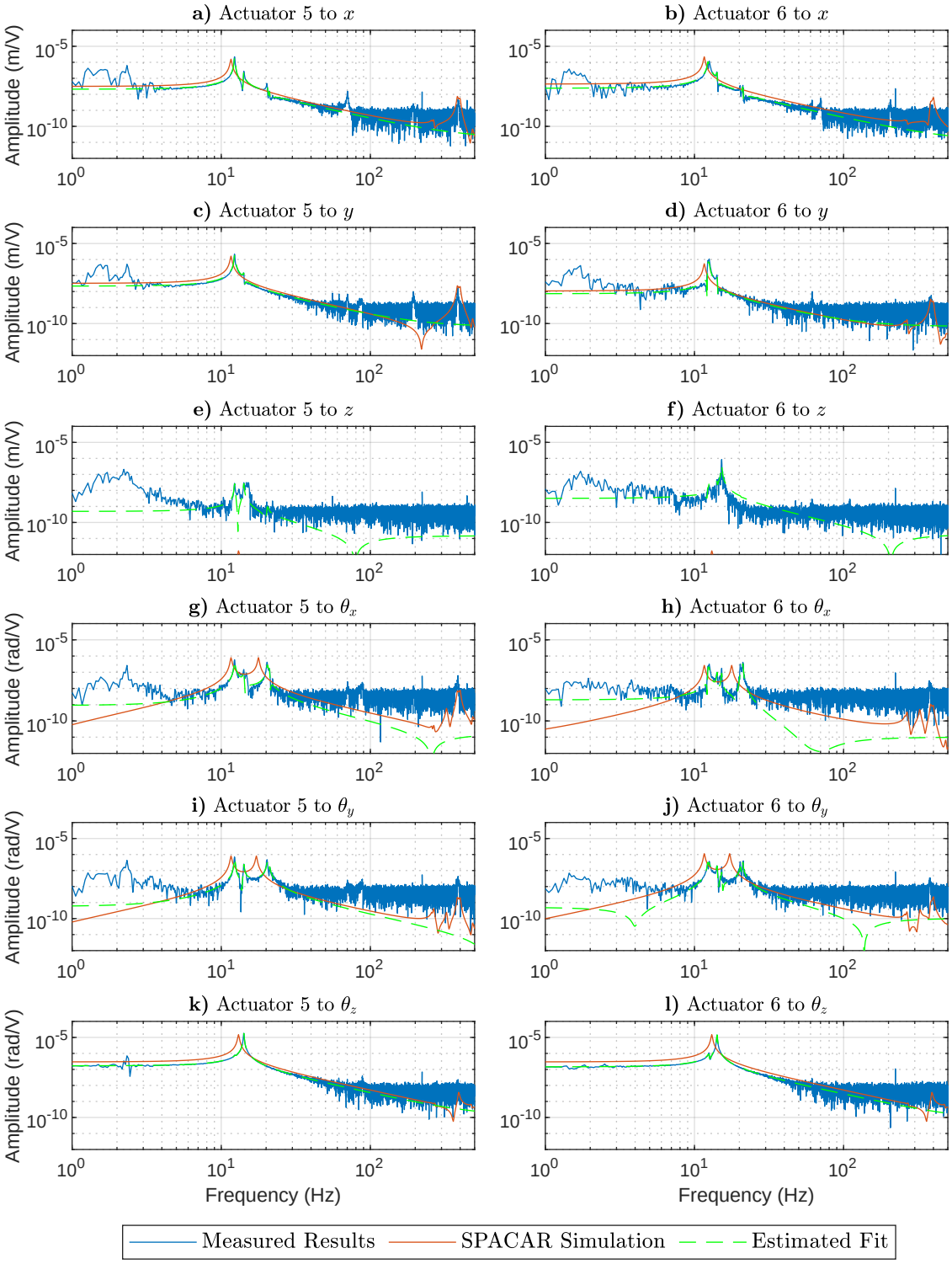

Figure A.2: System Response for Actuators 5 and 6